

REPORT DOCUMENTATION PAGE			Form Approved OMB NO. 0704-0188		
<p>The public reporting burden for this collection of information is estimated to average 1 hour per response, including the time for reviewing instructions, searching existing data sources, gathering and maintaining the data needed, and completing and reviewing the collection of information. Send comments regarding this burden estimate or any other aspect of this collection of information, including suggestions for reducing this burden, to Washington Headquarters Services, Directorate for Information Operations and Reports, 1215 Jefferson Davis Highway, Suite 1204, Arlington VA, 22202-4302. Respondents should be aware that notwithstanding any other provision of law, no person shall be subject to any penalty for failing to comply with a collection of information if it does not display a currently valid OMB control number.</p> <p>PLEASE DO NOT RETURN YOUR FORM TO THE ABOVE ADDRESS.</p>					
1. REPORT DATE (DD-MM-YYYY) 15-02-2018		2. REPORT TYPE Final Report		3. DATES COVERED (From - To) 1-Oct-2014 - 30-Sep-2017	
4. TITLE AND SUBTITLE Final Report: Production, Analysis and Control of Unsteady Vortical Wake-Airfoil Interactions: Harnessing the Unique Capabilities of Active Flow Control for Unsteady Aerodynamics Research			5a. CONTRACT NUMBER W911NF-14-1-0662		
			5b. GRANT NUMBER		
			5c. PROGRAM ELEMENT NUMBER 611102		
6. AUTHORS			5d. PROJECT NUMBER		
			5e. TASK NUMBER		
			5f. WORK UNIT NUMBER		
7. PERFORMING ORGANIZATION NAMES AND ADDRESSES University of Arizona P.O. Box 210158, Rm 510 Tucson, AZ 85721 -0158			8. PERFORMING ORGANIZATION REPORT NUMBER		
9. SPONSORING/MONITORING AGENCY NAME(S) AND ADDRESS (ES) U.S. Army Research Office P.O. Box 12211 Research Triangle Park, NC 27709-2211			10. SPONSOR/MONITOR'S ACRONYM(S) ARO		
			11. SPONSOR/MONITOR'S REPORT NUMBER(S) 64938-EG-YIP.5		
12. DISTRIBUTION AVAILABILITY STATEMENT Approved for public release; distribution is unlimited.					
13. SUPPLEMENTARY NOTES The views, opinions and/or findings contained in this report are those of the author(s) and should not be construed as an official Department of the Army position, policy or decision, unless so designated by other documentation.					
14. ABSTRACT					
15. SUBJECT TERMS					
16. SECURITY CLASSIFICATION OF:			17. LIMITATION OF ABSTRACT UU	15. NUMBER OF PAGES	19a. NAME OF RESPONSIBLE PERSON Jesse Little
a. REPORT UU	b. ABSTRACT UU	c. THIS PAGE UU			19b. TELEPHONE NUMBER 520-626-8677

RPPR Final Report

as of 26-Feb-2018

Agency Code:

Proposal Number: 64938EGYIP

Agreement Number: W911NF-14-1-0662

INVESTIGATOR(S):

Name: Ph.D Jesse Little
Email: jesselittle@email.arizona.edu
Phone Number: 5206268677
Principal: Y

Organization: **University of Arizona**

Address: P.O. Box 210158, Rm 510, Tucson, AZ 857210158

Country: USA

DUNS Number: 806345617

EIN: 866004791

Report Date: 31-Dec-2017

Date Received: 15-Feb-2018

Final Report for Period Beginning 01-Oct-2014 and Ending 30-Sep-2017

Title: Production, Analysis and Control of Unsteady Vortical Wake-Airfoil Interactions: Harnessing the Unique Capabilities of Active Flow Control for Unsteady Aerodynamics Research

Begin Performance Period: 01-Oct-2014

End Performance Period: 30-Sep-2017

Report Term: 0-Other

Submitted By: Ph.D Jesse Little

Email: jesselittle@email.arizona.edu

Phone: (520) 626-8677

Distribution Statement: 1-Approved for public release; distribution is unlimited.

STEM Degrees: 4

STEM Participants: 6

Major Goals: Unsteady aerodynamics research associated with vortex-body interactions (VBI) has a long history examining both isolated (vortices separated by a distance greater than the characteristic length scale of the body) and non-isolated (vortices separated by a distance less than the characteristic length scale of the body) encounters. In both cases, experimentally generating a vortex or train of vortices that approximates real-world flight conditions is non-trivial. Disturbance generators are typically based on mechanical devices (e.g., pitching/plunging airfoils) or fixed objects (e.g., bluff bodies). These studies have provided insight into important parameters governing VBI, but do not allow production of controlled disturbances at conditions relevant to many practical applications (e.g., rotorcraft, turbomachinery, etc). This work examines the use of active flow control (AFC), specifically nanosecond pulse driven dielectric barrier discharge (ns-DBD) plasma actuators, as an enabling technology for the study of VBI. Two NACA 0012 airfoils are employed to act as disturbance and target bodies. Ns-DBD plasma actuation is used on the leading edge of the disturbance airfoil at a Reynolds number of 740,000 (40 m/s) for a post-stall angle of 18°. Actuation is used to excite the wake giving rise to three flow regimes. Low-frequency forcing ($F^+ = f c / U < 0.15$ (20 Hz)) generates a single disturbance in the wake after which the flow relaxes back to something resembling the baseline state. Spectra acquired downstream ($x/c=6$) indicate the existence of a fundamental frequency along with multiple higher harmonics due to the impulse like nature of the flow response. The sign of the vortex in this case is dominantly positive (counter-clockwise) meaning it is shed from the pressure side of the disturbance airfoil. Forcing in the range of $0.3 < F^+ < 0.92$ ($40 < f < 120$ Hz) produces sinusoidal oscillations in the wake characterized by a single peak in the spectrum at the forcing frequency. Coherence spectra in the wake at $x/c=6$ indicate significant 2D features over the central half span of the wind tunnel (1.5 airfoil chord lengths) for these two regimes. In general, the wake can be excited at any frequency (up to $x/c=6$) provided it is near or below the onset of the inertial subrange. A further increase in forcing frequency results in separation control over the disturbance airfoil with no clear structure in the wake. $F^+ = 1.14$ (120 Hz) is found to be optimal for separation control in these conditions. The influence of forcing amplitude (i.e., ns-DBD pulse energy) is also explored, but hardware limitations did not allow decoupling of amplitude and frequency effects at this time. Limited VBI studies on the target airfoil indicate that the most extreme fluctuations of forces and moments are found for isolated encounters ($F^+ = f c / U_{wake} \approx 0.169$ (20 Hz)) with a highly loaded target (16° incidence). In this case, a significant viscous response is observed in which a separation bubble is formed and shed over the target airfoil's suction surface. This produces an abrupt increase and subsequent decrease in lift coefficient followed by another broader increase during the lift recovery. Increasing the frequency (non-isolated encounter) or decreasing the loading (lower AoA) eliminates this effect and generates a nearly sinusoidal fluctuation of the target airfoil's lift coefficient that could likely be modeled with potential flow. This research shows that AFC is an enabling technology for studies of VBI setting the stage for future work at an expanded range of Mach numbers, Reynolds numbers and

RPPR Final Report as of 26-Feb-2018

configurations.

Accomplishments: The capability of AFC, specifically ns-DBD plasma actuators, to enable the production of disturbances for studies of VBI has been investigated. Two identical instrumented NACA 0012 airfoils were fabricated to serve as disturbance (upstream) and target (downstream) bodies. The baseline lift coefficient for both airfoils was validated against thin airfoil theory and XFLR5. The disturbance airfoil was positioned at a post-stall angle of 18° . This decision was based on in-house experiments as well as literature suggesting a natural low frequency oscillation can be present in the wake at such conditions (Wu et al. 1998). Ns-DBD plasma actuators were used to excite the separated shear layer over the airfoil as well as the downstream wake. Low frequency forcing ($F^+ < 0.15$ (20 Hz)) generated a single vortical disturbance after which the flow relaxed back to something resembling the baseline state. The full re-establishment of the baseline separated flow condition was dependent on the frequency of forcing. More specifically, the lowest frequency case (e.g., $F^+ = 0.0375$ (5 Hz)) resembled an impulse response producing multiple higher harmonics in PSD measured at $x/c=6$ from the leading edge of the upstream airfoil. The sign of the vortex in these cases was dominantly positive (counter-clockwise) in the wake indicating it is shed from the pressure surface. Inspection of phase-averaged transverse velocity fluctuations and vorticity from $x/c=0$ to 4.5 showed that a negative region of vorticity (clockwise) is formed by severing the separated shear layer with a single pulse of actuation. However, this structure is weaker and shed into a higher region of the wake such that any VBI is dominated by the interaction of the target airfoil with a single vortex of positive sign (counter-clockwise). The effect of ns-DBD pulse amplitude was explored using single frequency forcing. Results were surprisingly similar to transient separation control studies published using other airfoils, actuators and forcing locations highlighting the robustness of the flow physics (in this case the flow instability) that governs response. A single pulse of actuation severs the separated shear layer resulting in a vortex of negative sign (clockwise) being shed into the wake. The separated flow then gradually re-establishes over approximately 10 convective times in a manner that resembles dynamic stall. Varying the amplitude of forcing by a factor of three did not have an appreciable effect on these observations. This indicates that the effect of frequency and amplitude cannot be decoupled in this particular study of AFC-enhanced VBI. However, this is presumed to be a limitation of the employed power supply rather than some fundamental barrier.

As the ns-DBD forcing frequency is raised ($0.3 < F^+ < 0.92$ ($40 < f < 120$ Hz)), the wake oscillations become sinusoidal. Transverse velocity fluctuations are highly organized into positive and negative patterns associated with a coherent train of vortices. This is also expressed in phase-averaged vorticity where pairs of counter-rotating vortices persist in the wake. PSD at $x/c=6$ show a single dominant peak consistent with this signal. A further increase in forcing frequency results in separation control over the disturbance airfoil with no clear structure in the wake. This is expected for a forcing frequency near $F^+ \approx 1$ based on knowledge of boundary layer separation control (Greenblatt and Wygnanski 2000) and the fact that the wake is not clearly excited is not surprising. All forcing frequencies have an influence on the time-average velocity and surface pressure, but it is clear throughout the data that $F^+ \approx 1.14$ (120 Hz) is optimal for separation control in these conditions. The time-average flow over the disturbance airfoil under the influence of AFC is reasonably two-dimensional over the central half-span based on surface pressure measurements. The coherence of AFC generated disturbances is found to reach levels well-above 0.5 at $x/c=6$ across the central half of the wake suggesting some level of 2D behavior. In general, the wake can be excited at any frequency (at least downstream to $x/c=6$) provided it is near or below the onset of the inertial subrange. More specifically, forcing below $F^+ < 0.15$ (20 Hz) produces a single disturbance that is dominated by positive vorticity and appears at the fundamental frequency and multiple harmonics in the PSD. The wake can be locked to a single frequency in the range ($0.3 < F^+ < 0.92$ ($40 < f < 120$ Hz)) characterized by sinusoidal behavior and a single peak in the PSD. At higher frequencies, the disturbance airfoil experiences boundary layer separation control and forcing is not relevant for AFC-enabled VBI studies.

VBI is explored for each of the previously mentioned forcing regimes. The effect of the baseline wake from the disturbance airfoil on the lift coefficient of the target airfoil is to eliminate the onset of hard stall presumably due to accelerated laminar-to-turbulent transition. A natural unsteadiness in Cl is found for this case near $St=0.635$ (75 Hz). Note that expressions of F^+ and St employ the characteristic velocity of the wake in reference to VBI studies here. Thus, the dimensionless frequencies are increased by 10% compared the case with a disturbance airfoil alone. The most compelling force and momentum fluctuations due to VBI on the target airfoil are found for isolated encounters ($F^+ \approx 0.169$ (20 Hz)) at high incidence (e.g., 16°). In this case, a clear viscous response is observed on the target airfoil that results in formation and shedding of a separation bubble. This produces an abrupt increase and subsequent decrease in lift coefficient followed by another broader increase during the lift recovery. The cause of the latter is still under investigation. PSD of Cl show a peak at the fundamental frequency along with multiple higher harmonics. Increasing the frequency (non-isolated encounter) or decreasing the loading (lower AoA) eliminates this effect and generates nearly sinusoidal behavior of the target airfoil lift coefficient that could likely be modeled with potential flow. The upwash and downwash produced by the various vortices is quite clear from phase-averaged PIV and explains the variations in Cl in most cases.

RPPR Final Report

as of 26-Feb-2018

Training Opportunities: MS Theses

1. T. Ashcraft, "Control of Boundary Layer Separation and the Wake of an Airfoil using Ns-DBD Plasma Actuators," MS Thesis, Aerospace and Mechanical Engineering, University of Arizona, 2016.
2. C. Durasiewicz, "Comparison of Transitory Separation Control over an Airfoil using Ac-DBD and Ns-DBD Plasma Actuators," MS Thesis, TU Berlin, 2017.
3. A. Weingaertner, "Parallel Vortex Body Interaction Enabled by Active Flow Control," MS Thesis, TU Berlin, expected 2018.

Students Supported

T. Ashcraft, MS 2016 (external support)
C. Durasiewicz, MS 2017
A. Singh, PhD expected 2019 (partial support)
A. Weingaertner, MS expected 2018

Results Dissemination: Conference Abstracts

1. C. Durasiewicz, J. Maldonado and J. Little, "Active Control of Airfoil Boundary Layer Separation and Wake using Ns-DBD Plasma Actuators," 69th American Physical Society, Division of Fluid Dynamics Meeting, Portland, OR, November 21, 2016; Bulletin of the American Physical Society, Vol. 61, No. 20.

Conference Papers

1. T. Ashcraft, K. Decker and J. Little. "Control of Boundary Layer Separation and the Wake of an Airfoil using ns-DBD Plasma Actuators", 54th AIAA Aerospace Sciences Meeting, AIAA SciTech Forum, (AIAA 2016-0839).
2. C. Durasiewicz, A. Singh and J. Little. "A Comparative Flow Physics Study of Ns-DBD vs Ac-DBD Plasma Actuators for Transient Separation Control on a NACA 0012 Airfoil", 2018 AIAA Aerospace Sciences Meeting, AIAA SciTech Forum, (AIAA 2018-1061)
3. A. Weingaertner, P. Tewes and J. Little. "Parallel Vortex Body Interaction Enabled by Active Flow Control", submitted to the 2018 AIAA Aviation Meeting.

Journal Articles

1. T. Ashcraft, C. Durasiewicz, A. Singh, K. Decker and J. Little, "Airfoil Post-Stall Flow Control using ns-DBD Plasma Actuation (tentative)" in preparation for submission to Experiments in Fluids, 2018.

Honors and Awards: Nothing to Report

Protocol Activity Status:

Technology Transfer: Nothing to Report

PARTICIPANTS:

Participant Type: PD/PI

Participant: Jesse Little

Person Months Worked: 1.00

Funding Support:

Project Contribution:

International Collaboration:

International Travel:

National Academy Member: N

Other Collaborators:

CONFERENCE PAPERS:

RPPR Final Report
as of 26-Feb-2018

Publication Type: Conference Paper or Presentation **Publication Status:** 1-Published
Conference Name: AIAA SciTech 2016
Date Received: 31-Aug-2016 Conference Date: 04-Jan-2016 Date Published: 01-Feb-2016
Conference Location: San Diego, CA
Paper Title: Control of Boundary Layer Separation and the Wake of an Airfoil using ns-DBD Plasma Actuators
Authors: Timothy Ashcraft, Kenneth Decker, Jesse Little
Acknowledged Federal Support: Y

Publication Type: Conference Paper or Presentation **Publication Status:** 1-Published
Conference Name: AIAA SciTech 2018
Date Received: 15-Feb-2018 Conference Date: 08-Jan-2018 Date Published: 08-Jan-2018
Conference Location: Orlando, FL
Paper Title: A Comparative Flow Physics Study of Ns-DBD vs Ac-DBD Plasma Actuators for Transient Separation Control on a NACA 0012 Airfoil
Authors: Claudia Durasiewicz, Ashish Singh, Jesse Little
Acknowledged Federal Support: Y

DISSERTATIONS:

Publication Type: Thesis or Dissertation
Institution: University of Arizona
Date Received: 31-Aug-2016 Completion Date: 3/1/16 11:35PM
Title: CONTROL OF BOUNDARY LAYER SEPARATION AND THE WAKE OF AN AIRFOIL USING NS-DBD PLASMA ACTUATORS
Authors: Timothy Ashcraft
Acknowledged Federal Support: Y

Publication Type: Thesis or Dissertation
Institution: TU Berlin
Date Received: Completion Date: 9/5/18 6:44AM
Title: Comparison of Transitory Separation Control over an Airfoil using AC-DBD and ns-DBD Plasma Actuators
Authors: Claudia Durasiewicz
Acknowledged Federal Support: Y

Final Report

Production, Analysis and Control of Unsteady Vortical Wake-Airfoil Interactions: Harnessing the Unique Capabilities of Active Flow Control for Unsteady Aerodynamics Research (YIP 2014)

**Army Research Office
Contract Number: W911NF-14-1-0662
Program Manager: Dr. Matthew Munson**

**Jesse Little
Associate Professor
Department of Aerospace and Mechanical
Engineering
University of Arizona**

February 2018

I. Abstract

Unsteady aerodynamics research associated with vortex-body interactions (VBI) has a long history examining both isolated (vortices separated by a distance greater than the characteristic length scale of the body) and non-isolated (vortices separated by a distance less than the characteristic length scale of the body) encounters. In both cases, experimentally generating a vortex or train of vortices that approximates real-world flight conditions is non-trivial. Disturbance generators are typically based on mechanical devices (e.g., pitching/plunging airfoils) or fixed objects (e.g., bluff bodies). These studies have provided insight into important parameters governing VBI, but do not allow production of controlled disturbances at conditions relevant to many practical applications (e.g., rotorcraft, turbomachinery, etc). This work examines the use of active flow control (AFC), specifically nanosecond pulse driven dielectric barrier discharge (ns-DBD) plasma actuators, as an enabling technology for the study of VBI. Two NACA 0012 airfoils are employed to act as disturbance and target bodies. Ns-DBD plasma actuation is used on the leading edge of the disturbance airfoil at a Reynolds number of 740,000 (40 m/s) for a post-stall angle of 18° . Actuation is used to excite the wake giving rise to three flow regimes. Low-frequency forcing ($F^+ = fc/U_\infty < 0.15$ (20 Hz)) generates a single disturbance in the wake after which the flow relaxes back to something resembling the baseline state. Spectra acquired downstream ($x/c=6$) indicate the existence of a fundamental frequency along with multiple higher harmonics due to the impulse like nature of the flow response. The sign of the vortex in this case is dominantly positive (counter-clockwise) meaning it is shed from the pressure side of the disturbance airfoil. Forcing in the range of $0.3 < F^+ < 0.92$ ($40 < f < 120$ Hz) produces sinusoidal oscillations in the wake characterized by a single peak in the spectrum at the forcing frequency. Coherence spectra in the wake at $x/c=6$ indicate significant 2D features over the central half span of the wind tunnel (1.5 airfoil chord lengths) for these two regimes. In general, the wake can be excited at any frequency (up to $x/c=6$) provided it is near or below the onset of the inertial subrange. A further increase in forcing frequency results in separation control over the disturbance airfoil with no clear structure in the wake. $F^+=1.14$ (120 Hz) is found to be optimal for separation control in these conditions. The influence of forcing amplitude (i.e., ns-DBD pulse energy) is also explored, but hardware limitations did not allow decoupling of amplitude and frequency effects at this time. Limited VBI studies on the target airfoil indicate that the most extreme fluctuations of forces and moments are found for isolated encounters ($F^+ = fc/U_{wake} \leq 0.169$ (20 Hz)) with a highly loaded target (16° incidence). In this case, a significant viscous response is observed in which a separation bubble is formed and shed over the target airfoil's suction surface. This produces an abrupt increase and subsequent decrease in lift coefficient followed by another broader increase during the lift recovery. Increasing the frequency (non-isolated encounter) or decreasing the loading (lower AoA) eliminates this effect and generates a nearly sinusoidal fluctuation of the target airfoil's lift coefficient that could likely be modeled with potential flow. This research shows that AFC is an enabling technology for studies of VBI setting the stage for future work at an expanded range of Mach numbers, Reynolds numbers and configurations.

II. Table of Contents

I.	Abstract	2
II.	Table of Contents	3
III.	Introduction	4
IV.	VBI Background	5
	A. General Classifications	5
	B. Isolated Encounters	7
	C. Non-isolated Encounters	8
	D. Modeling and Simulation	10
	E. Summary	12
V.	Experimental Facilities and Techniques	12
	A. Wind tunnel	12
	B. Airfoil Models	13
	C. Instrumentation	13
	D. DBD Plasma Actuators	14
VI.	Results	16
	A. Airfoil Characterization	16
	B. Boundary Layer Separation and Wake Control	17
	a. Test Conditions 17	
	b. Pressure Measurements 17	
	c. PIV Results 19	
	d. Constant Temperature Anemometry 22	
	C. Transient Behavior	24
	D. Vortex Body Interaction	27
VII.	Summary and Conclusions	34
VIII.	Future Work	36
IX.	Publications and Students	36
X.	Acknowledgements	37
XI.	References	37

III. Introduction

Unsteadiness is present in many flows of high interest to the Army spanning both rotary and fixed wing platforms. Rotorcraft and turbomachinery performance are particularly dependent on the response of aerodynamic surfaces to unsteady and vortex dominated flows. Fixed wing unmanned air vehicles (UAVs) can also operate in unsteady environments (especially at low altitudes), in urban settings and during formation flight. Future generations of both rotary and fixed wing aircraft will encounter progressively more challenging unsteady flight regimes as autonomous systems mature.

Classical unsteady aerodynamics (e.g. Kussner, Loewy, Miles, Sears, Theodorsen, Wagner, etc.) provides analytical solutions for a variety of conditions (Leishmann 2000). Such treatments give substantial insight, but are not capable of predicting viscous effects like partially separated or stalled conditions. Phenomena like dynamic stall and vortex-body interaction (VBI) create additional complexities. These flows not only generate unsteadiness, but can operate in the midst of unsteadiness from preceding blades, components and/or naturally occurring flight environments. Vortex wake models of varying complexity have been developed, but relating these to time dependent viscous effects remains challenging and often intractable at high Reynolds number (Re). These difficulties are not isolated to theoretical and computational approaches. Reasonable scale experimental efforts that produce relevant interactions between flow unsteadiness, vortical wakes and aerodynamic surfaces including viscous effects are often limited to large-scale wind tunnel or flight tests that are not appropriate for fundamental and systematic investigation.

This work addresses the production, analysis and prospective control of VBI using active flow control (AFC) as an enabling technology. An upstream airfoil is placed in stall and AFC is used to produce disturbances in the wake. The interaction of these vortical wakes with a downstream target airfoil is studied as a function of the disturbance frequency and target airfoil loading (i.e., AoA). This research is unique in that it produces controlled unsteady vortical wakes over a wide range of frequencies. In doing so, it is possible to explore the boundary between isolated and non-isolated encounters as well as the demarcation between viscous and inviscid phenomena. The unsteadiness generation technique is based on the use of nanosecond pulse driven dielectric barrier discharge (ns-DBD) plasmas for separation control. Ns-DBD plasma actuators differ from more commonly studied ac-DBDs in that the control mechanism relies on thermal energy deposition rather than momentum generation. In previous efforts, ns-DBD plasma was used as a flow control actuator for delaying static airfoil stall (Rethmel et al. 2011; Little et al. 2012). However, an interesting observation was that the ns-DBD could initiate vortex formation in the airfoil wake over a substantial bandwidth up to Re and Mach numbers of 1.15×10^6 and 0.26 respectively. This presumably high amplitude capability is appealing from a flow control actuator perspective, but can also be used as a tool for producing controlled VBIs between vortical wakes and a downstream target body. This research evaluates these capabilities and sets the stage for modeling, sensing and control of flows that possess significant unsteady components in bandwidth and Re ranges that have not been adequately addressed to date. More generally, it provides a platform for fundamental and systematic studies of flow physics and control associated with VBIs.

This research has two primary objectives: 1) Develop and characterize an experimental AFC-based method for producing unsteady vortical wakes of practical interest; 2) Analyze the basic physics and establish the governing parameters that dictate the aerodynamic response of lifting surfaces immersed in these unsteady flows with specific focus on the importance (or lack thereof) of viscous effects. Applied systems such as rotorcraft and turbomachinery will find this study and its outcomes of significant use. For example, the foundations of active boundary layer separation control technology are based on fixed wing systems that generally operate in low to moderate turbulence environments. Dynamic stall has also primarily been studied using oscillating airfoils subject to uniform and steady inflow conditions. This work provides the capability to study representative flow conditions for unsteady flight environments that have not been simulated in experiments and computations to date. In particular, flows related to rotorcraft maneuvers, dynamic stall, blade vortex interaction and turbine clocking can be explored in a controlled

fashion through variation of frequency content in the approaching wake. It also provides further insight into the capabilities and mechanisms of pulsed plasma actuators for AFC in general.

IV. VBI Background

A. General Classifications

The interaction of a vortex with an infinite solid wall (vortex-wall interaction) has been reviewed by Doligalski and Walker (1984). Important parameters governing the response include the vortex proximity and vortex Reynolds number ($Re_v = \Gamma/2\pi\nu$, where Γ is the vortex circulation and ν is kinematic viscosity). For high Re_v in close proximity, a viscous response is observed in which boundary layer eruption generates new vortices with similar strength. At lower Re_v , these events may be weak or not present at all (inviscid response). Features of the viscous response are seemingly general and vortex-induced separation is observed for many types of interactions due to the travelling adverse pressure gradient felt by the wall. A relatively simple potential flow model for a 2D vortex convecting in a uniform flow above a wall can give insight into the general flow features, but cannot capture details of the viscous response (Doligalski and Walker 1984). Eruption events also occur for 3D cases, but are more complex often culminating in hairpin type structures. An example of 3D interactions is the necklace vortex formed at the base of a cylinder. In this case, the eruption events are created by vortices with streamwise orientation.

Vortex-wall interactions are important in processes such as dynamic stall in rotorcraft, turbomachinery and wind turbines during the formation and development of the dynamic stall vortex. In these cases, the unsteady motion of the lifting surface produces the vortex and subsequent boundary layer interaction. This is in contrast to the previous description in which the structure is produced by some static geometry (e.g., necklace vortex) or from some upstream disturbance that results in a vortex convecting in an otherwise uniform flow.

The general interaction of a vortex with a body can produce unsteady loading and heat transfer, noise, vibration and other detrimental or even beneficial effects. Such events are a subset of more general turbulence-body interactions. These are prevalent in rotorcraft, turbomachinery and propeller driven fixed-wing aircraft, but can also occur in canard-wing interactions and UAVs in unsteady environments or formation flight. These vortex-body interactions are typically classified according to their relative orientations Figure 1. This work focuses on the parallel interaction (Figure 1a), but future studies of skewed and other more complex 3D orientations are feasible. The unsteady loading, associated boundary layer separation and its control when the target body is a lifting surface are of particular interest.

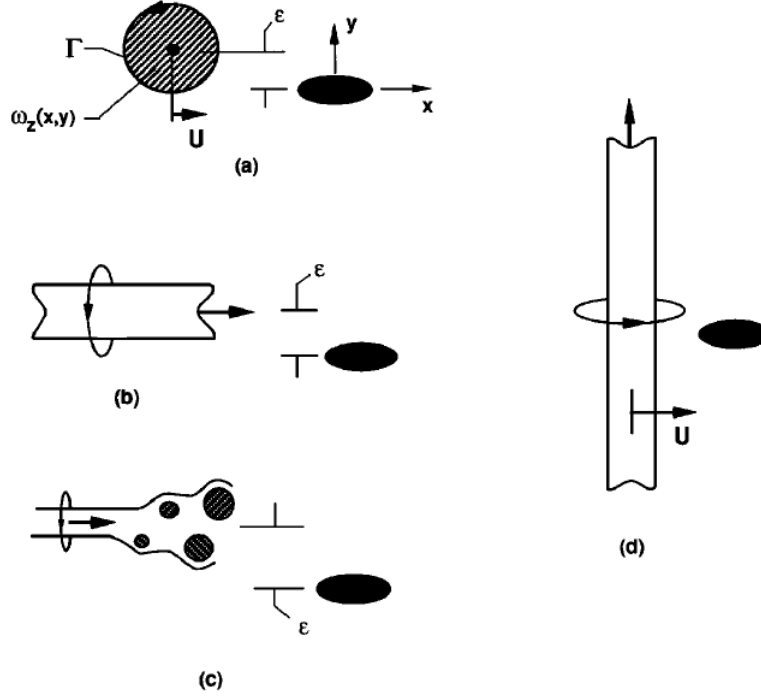


Figure 1: Basic classes of vortex-body interaction: a) parallel, b) perpendicular without breakdown, c) perpendicular with breakdown and d) normal (Rockwell 1998).

If the vortex is sufficiently far from the surface, the interaction can be similar to the infinite wall case in which loading is primarily dependent on the circulation with only weak vortex distortion. For this scenario, simulations using rectilinear vortices have been successful in a variety of applications including boundary layer eruptions and Karman street interactions (Rockwell 1998). For a near-miss, the vortex becomes distorted and the circulation, vorticity distribution and the wavelength (for example in the case of Karman Street) must be considered. A strong impulsive loading can occur if the vortex directly impinges on a leading edge such that it is sliced by the body. Parallel vortex-body interactions are usually treated as quasi-2D, but longitudinal vorticity may be embedded in nominally spanwise vortices. An example is the cylinder wake which is known to contain such structures even in the turbulent case (Williamson 1996). The scales of vorticity may be such that they produce changes in unsteady loading on the body in question. The addition of 3D effects complicates both measurements and computations for this flow field which is already time-dependent and often at high Re in practice.

The importance of vortex interactions with lifting surfaces has long been recognized often in relation to rotorcraft. Many studies focus on producing an isolated encounter which is relevant for noise generation during blade-vortex interactions (BVI) in which the vorticity is shed from the rotor blade tip. These interactions can be parallel or perpendicular depending on the blade azimuth and flight regime. Figure 2 shows a situation of interest for parallel interactions. In studies focused on an isolated, parallel encounter, it is often challenging to produce the appropriate vortex. An isolated encounter is generally defined for vortices separated by a distance greater than the target airfoil chord (Booth and Yu 1986).

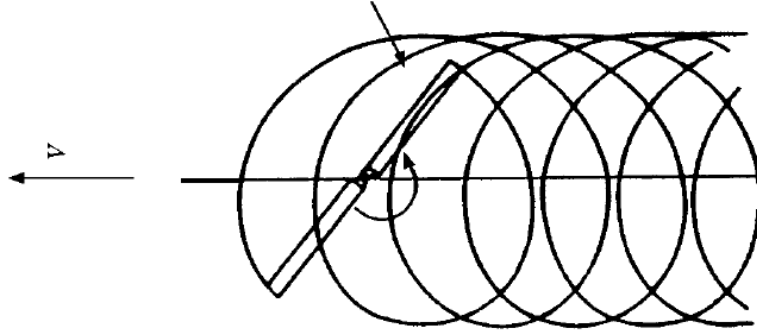


Figure 2: Schematic of blade interaction with tip vortices during an advancing, but descending approach (Wilder and Telionis 1998).

B. Isolated Encounters

Shock tubes have been used to study interaction between the starting vortex from an upstream disturbance airfoil and a downstream target airfoil (Meier and Timm 1985; Lee and Bershader 1994). Lee and Bershader (1994) used this experiment with a focus on noise generation. The convecting vortex was characterized in detail using independent measurements of density and pressure. The appropriate length scale for noise generation was suggested to be the target airfoil leading edge radius, rather than the airfoil chord and significant viscous effects were observed for strong head-on interactions in both experiments and computations. Horner et al. (1996) systematically varied the vortex strength and location relative to the target with specific focus on rotorcraft applications. In this case, the convecting vortex was generated by an upstream disturbance wing and interacted with an untwisted, non-lifting, single-blade target rotor. This early particle image velocimetry (PIV) study built upon similar experiments that contained only pressure data. The aerodynamic response of the target blade was primarily dependent on the effective incidence produced by the vortex (i.e. loading) as well as near surface interactions from it and/or its fragments after a head-on encounter. Secondary vortices were found to have a significant effect near the trailing edge. The authors point out the importance of using a representative lifting surface (i.e., with trailing edge) for rotorcraft aerodynamics studies.

Most methods of producing isolated encounters employ mechanical devices controlling an upstream airfoil to produce impulsive motion (Seath et al. 1989; Booth 1990; Straus et al. 1990; Wilder and Telionis 1998). Booth (1990) used such a device to produce isolated vortices separated by approximately five blade chords with focus on direct or near-miss encounters. Flow visualization at $Re=161,000$ showed target blade loading affected the vortex trajectory, convection velocity and core distortion. This was accompanied by oscillations in the target airfoil leading edge suction peak. Transient loads were increased with increasing target airfoil incidence (i.e. steady loading) and near vortex-airfoil proximity. The greatest lift changes were observed for a direct encounter between the vortex and leading edge. (Straus et al. 1990) examined an isolated encounter with a symmetric airfoil at zero incidence for $Re=210,000$. Inviscid theories were evaluated and found to be lacking even for an unloaded airfoil unless the vortex was far away or rotating such that it accelerated the boundary layer on the facing surface. Vortex-induced separation, when observed, persisted until the convecting structure was well-downstream of the trailing edge.

Wilder and Telionis (1998) published a detailed water tunnel study with phase-averaged laser doppler velocimetry (LDV) at low Re (19,000). Pressure gradients in x and y were evaluated using measured quantities and the Navier-Stokes equations under a 2D assumption. No vortex-induced separation was observed at zero incidence, but a loaded blade showed characteristics somewhat similar to dynamic stall. In this case, the convecting vortex and the shed vortex (which were counter-rotating) propagated over the airfoil without disintegration in part due to mutual induction (Figure 3). Tip vortex formation in general has been observed for a variety of target bodies with both sharp and round leading edges (Rockwell 1998). The occurrence is dependent on the scale and circulation of the incident vortex relative to the leading edge radius. The sign, impingement location and loading on the target body are also influential. Wilder and

Telionis (1998) observed that a direct encounter of the vortex with the leading edge resulted in disintegration into much weaker structures in agreement with observations for a Karman street (Gursul and Rockwell 1990) and a thin flat plate shorter than $\frac{1}{4}$ the vortex core (Swirydzuk et al. 1993). Vortex signature was confirmed as an abrupt wall pressure fluctuation that progresses downstream along with the structure. The downstream propagation was accompanied by decreasing amplitude in the unloaded case. For interactions at incidence, the pressure signature near the leading edge was initially sharp, but eventually broadened and weakened consistent with vortex break-up. Very little pressure amplitude decrease along the chord was observed in the case of a counterclockwise vortex propagating over the loaded suction surface at positive incidence (Figure 3). The rotational direction and impingement location of the convecting vortex was noted to be an important parameter affecting the boundary layer response.

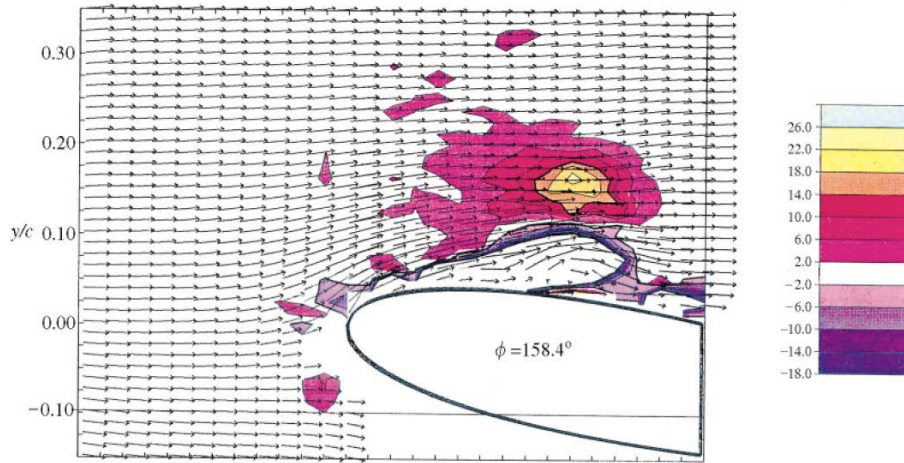


Figure 3: LDV data for interaction of a counterclockwise vortex with the suction side of an airfoil at positive incidence (Wilder and Telionis 1998).

C. Non-isolated Encounters

Encounters with vortices having spacing of less than the target body length scale have also been examined. Common methods for producing such disturbances employ mixing layers, bluff-body wakes and oscillating airfoils with a target body placed downstream. The natural instability in a mixing layer produces vortices of the same sign. A practical example is the corner impingement observed in cavity flow. The Karman vortex street present in a wake is composed of alternating vortices with different sign. Oscillating airfoils that shed vortices from the trailing edge are similar to a Karman vortex street, but with different rotational sense and lower background turbulence levels. If the oscillating airfoil proceeds through dynamic stall (leading edge shedding), a pattern more similar to the bluff body is recovered.

Various wake flows have been employed for parallel interactions. Meier and Timm (1985) employed a shock tube with a square cylinder upstream of a target airfoil for high subsonic flows at $Re=200,000-300,000$. In a very illustrative study, Gursul and Rockwell (1990) placed an elliptical leading edge in the wake of a shedding plate in water. The interaction was governed by the vortex and body length scales, circulation, wavelength and proximity of the street with respect to the body. The vortex wavelength and size was varied using different plate thicknesses. No boundary layer separation was observed in these tests due to the low Re_v and unloaded target. Small and large-scale interactions were defined by the ratio of wavelength to body half-thickness. Figure 4 presents sample flow visualization and pressure measurements for a small-scale interaction. Note the oscillatory surface pressure corresponding to the vortex location and rotational direction. For example, at $x/H=0.5$ a strong suction peak (p') is observed from boundary layer acceleration due to vortex rotation. The opposite effect is observed at approximately $x/H=1.5$ due to the different sign of rotation.

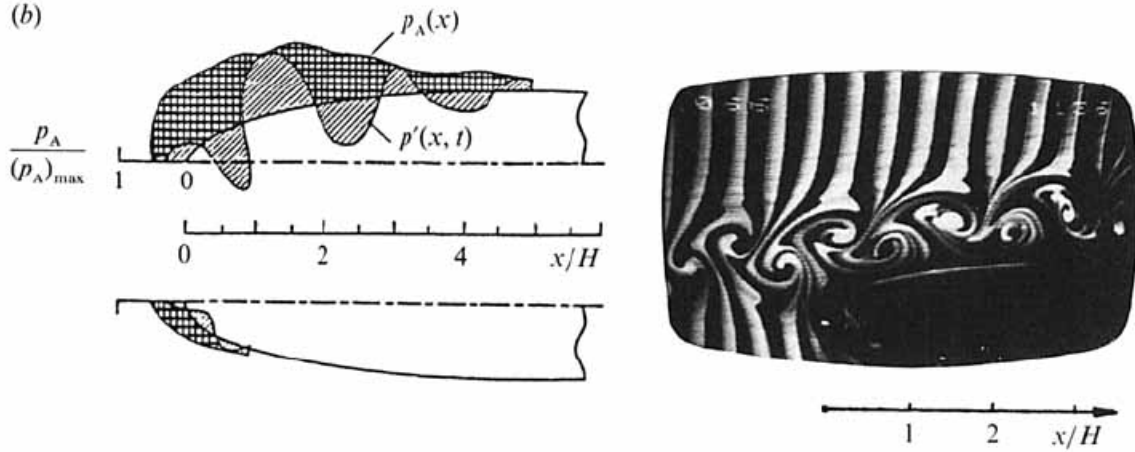


Figure 4: Unsteady pressure field and flow visualization for a Karman vortex street interacting with an elliptical leading edge. $P_A(x)$ corresponds to pressure amplitude while $p'(x, t)$ is the instantaneous pressure at the same instant as the flow visualization (Gursul and Rockwell 1990).

Vortical wakes from airfoils with sinusoidal motion (in contrast to impulsive motion) have also been studied. The flow can be composed of alternating vortical and potential flow regions. The frequency and amplitude of oscillation provides some control over the existence and properties of these regions. Maresca and Favier (1984) and Favier et al. (1985) longitudinally oscillated the disturbance airfoil through dynamic stall conditions such that vortices were shed from both the leading and trailing edge. Booth and Yu (1986) used an oscillation schedule where vortices originated primarily near the trailing edge. The potential advantage in these cases is that background turbulence levels are generally lower in comparison to bluff-body shedding. This dual airfoil arrangement can also be employed as a wave or Schmidt propeller. Rival et al. (2010) examined the low Re case (30,000) targeting MAV applications where the disturbance airfoil was oscillated in pure plunge. Loads were calculated based on control volume analysis and pressure-integration from PIV measurements similar to Wilder and Telionis (1998). The interaction was primarily governed by target airfoil loading rather than vertical spacing relative to the vortical wake. Observations were in general agreement with Wilder and Telionis (1998) despite the differences in disturbance generation. Figure 5 shows a sample vorticity field calculated from PIV data.

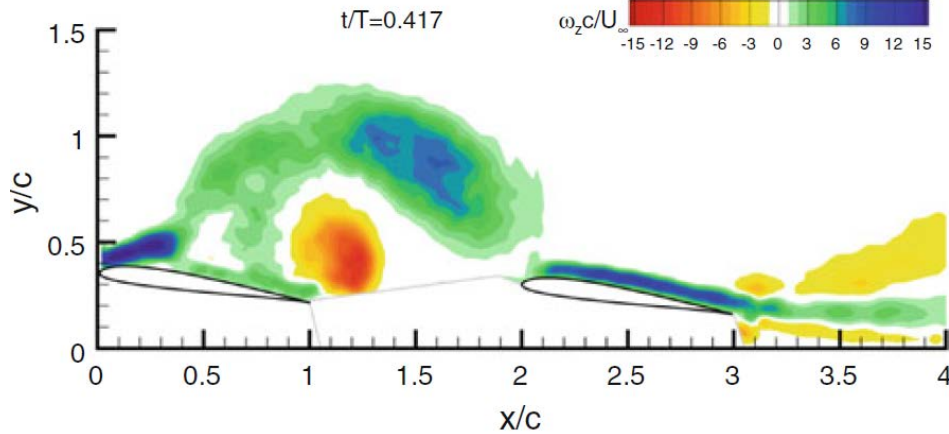


Figure 5: Parallel vortex interaction with a loaded lifting surface at $Re=30,000$ in Schmidt propeller arrangement (Rival et al. 2010).

The case of two airfoils both performing oscillations has been examined by Lee (2011) at $Re=85,000$. Two airfoils were positioned in series and oscillated in pitch at the same conditions, but with phase difference of 0° and 180° . The axial spacing between the models was also studied. In contrast to the previous examples, large coherent vortices were not generated meaning the interactions were primarily driven by the turbulent wake. A representative vorticity field calculated from PIV data is shown in Figure 6. Downwash from the disturbance airfoil prevented leading edge vortex formation on the target airfoil. Thus, C_l hysteresis was reduced in comparison to the baseline case (i.e., single airfoil). At zero phase delay, the C_l values increased with increasing axial spacing of the airfoils, but the opposite was observed for 180° phase shift. The aerodynamic performance of the phase shifted case generally outperformed zero phase shift throughout the test matrix.

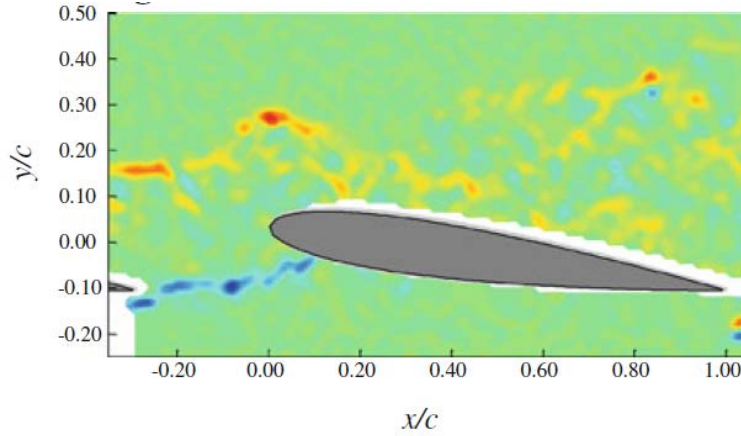


Figure 6: Sample target airfoil vorticity field calculated from PIV for a case with zero phase delay at 9° incidence during down stroke (Lee 2011).

D. Modeling and Simulation

Modeling and simulation efforts of varying complexity have been employed for parallel VBI. Lifting line theories are adequate provided the isolated vortex remains over one chord length from the blade (Poling et al. 1989). In general, inviscid predictions are favorable provided vortices remain far from the body and weak enough such that no viscous response is observed. Tucker and Conlisk (1992) used inviscid analysis and a large-scale vortex with constant vorticity to study Karman street impingement on a wedge. Vortex deformation was consistent with flow visualization suggesting the viscous aspects were not crucial. It should be noted that the vortex strength was weak and the wedge was under no steady loading. Various distributions of discrete vortices were studied by Panaras (1987) to investigate the effects of finite area during encounters with an airfoil (Figure 7a-c). The size of the vortex did not have a strong effect on the induced pressure provided the distance from the model was large. Vortices in closer proximity were substantially distorted which had a significant effect on the pressure field depending on the chosen distribution. A point vortex generated higher amplitude surface pressures in comparison to the distributed case (see Figure 7a-c). Modeling a direct encounter using point vortices was particularly erroneous.

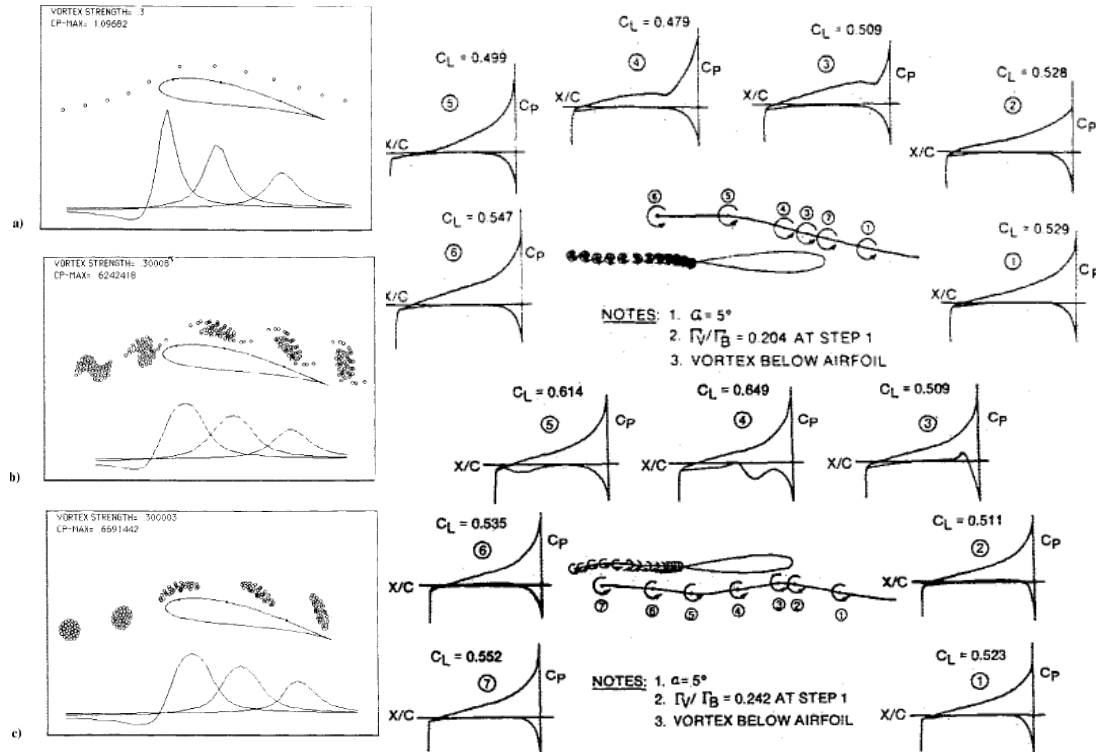


Figure 7: Unsteady pressure coefficients (isolated from mean flow) predicted by a point vortex (a), four rows of discrete vortices of small strength (b) and discrete vortices arranged in a circle (c) (Panaras 1987). Instantaneous pressure distribution from 2D model for 5° incidence NACA 0012 with vortex passing over suction (d) and pressure surfaces (e) (Poling et al. 1989).

Poling et al. (1989) used a single discrete vortex encountering an airfoil and enforced an unsteady Kutta condition at the trailing edge (Figure 7d,e). Temporal fluctuations in lift were accurately predicted for the cases surveyed, but vortex distortion due to a direct leading edge encounter was not considered. In the case of a direct encounter, a strong distortion or even splitting of the vortex can occur. Not surprisingly, the loading due to this interaction cannot be captured using quasi-steady analysis (Lee and Smith 1991). It was noted that lift fluctuations occurred on a time scale much shorter than those associated with vortex propagation from the leading to trailing edge which may give insight into methods of control. Indeed, unloading the blade just prior to interaction has been suggested as a strategy for reducing interaction strength (Wilder and Telonis 1998). Yao and Liu (1998) developed a time domain method to treat all classes of inviscid interactions. Special treatment was given to the vortex impingement case and the model was verified against classical unsteady aerodynamics theory. A broad class of interactions, including the Schmidt propeller, was examined with some success.

Studies that employ Euler or Navier-Stokes solvers, direct numerical simulations (DNS) or analytical methods exist, but are less common. Vortex distortion, viscous effects and flow separation have been computed for strong interactions, but were underpredicted in comparison to experiments (Lee and Bershader 1994). Hardin and Lamkin (1987a) used an Euler code for prediction of noise during the interaction between a distributed vortex and a Joukowski airfoil. They also produced a simple theoretical method for predicting the severity of noise during a parallel interaction (Hardin and Lamkin 1987b). The radiated noise was related to the vortex circulation, lift, span of the 2D interaction and miss distance. The importance of the target airfoil loading was captured by this relatively simple model and motivated some of the detailed experiment work referenced above. A relationship between unsteady loading and vortex distortion for incompressible viscous flow was produced by Howe (1995). This allows the loading to be

calculated in terms of only the velocity and vorticity distribution providing insight into the interpretation of spatially resolved experimental and computational data. More recently, Merrill and Peet (2017) examined the interaction between a shedding cylinder wake and a downstream pitching NACA 0012 airfoil using DNS at $Re=44,000$. Dynamic stall was delayed to a larger angle of attack and peaks in lift, drag and pitching moment coefficient were reduced in the presence of the cylinder wake. This was due, in part, accelerated laminar to turbulent transition in the boundary layer and separated shear layer.

E. Summary

The study of VBI has a long history and this brief review provides only a sample relevant to the conducted work. In all experimental cases, the disturbances are produced by a fixed body or a body undergoing some mechanical oscillation. Thus, the frequency of disturbances is limited by the body shape or mechanical system respectively. Experiments have been performed in water and air at relatively low Re_c ($<300,000$). Very few of these cases employ spatially-resolved diagnostics (PIV, LDV, etc.) and those that do are limited to even lower Re_c (max 85,000) which is less relevant to many Army applications.

It is clear that inviscid models are adequate provided the vortex is far from the body and does not overly disturb the pressure distribution so as to promote significant boundary layer thickening or separation. More complex interactions for strong vortices in close proximity or direct contact with the body at high Re remain challenging to compute. Skewed interactions that possess significant three-dimensionality are less common both in computations and experiments for obvious reasons. Active control of VBI from an aerodynamic perspective is much less-advanced in comparison to those of turbulent shear flows such as jets, wakes, mixing layers, boundary layers, etc.

The response of the target body is governed by many factors including vortex strength/size/distribution, proximity to target, target loading and wavelength in the case of a non-isolated encounter. It may be possible to characterize these effects by introducing dimensionless variables such as Re_c , Re_v , St and ratios of vortex size and proximity to some target body length scale. However, a primary factor governing the interaction is the target airfoil loading which is directly related to the response of the boundary layer to the pressure gradient imposed by the vortex. In the case of a non-isolated encounter, the frequencies present in the vortical wake could play a major role especially when the target airfoil boundary layer is susceptible to flow separation. These effects could be beneficial or detrimental depending on the vortex and boundary layer characteristics and have not been studied in detail. The lack of highly-resolved experimental data at high Re across a broad range of disturbance conditions places fundamental limitations on the understanding and control of these complex flows.

In the following sections, the experimental facility and AFC-based disturbance generation technique are described in detail. This is followed by an assessment of the wake behavior based on variations of both the frequency and amplitude of the applied AFC. Finally, preliminary studies of VBI on a downstream target airfoil are explored.

V. Experimental Facilities and Techniques

A. Wind tunnel

Experiments are performed in the University of Arizona AME subsonic wind tunnel. The wind tunnel is a closed loop facility with a 0.9 m x 1.2 m x 3.65 m (3 ft x 4 ft x 12 ft) test section. The speed of the flow in the tunnel can be varied up to $U_\infty = 80$ m/s (262.467 ft/s). Mean flow uniformity is better than $\pm 0.5\%$ across the operating range. Temperature in the tunnel is held within 0.44°C (1 °F) of a set point controlled by the operator using a heat exchanger with chilled water supply. Over its operating range, the turbulence intensity is less than 0.15% for $f_{lowpass} = 10$ kHz and less than 0.05% for $f_{bandpass} = 1\text{ Hz} - 10\text{ kHz}$. Above the test section, a two-axis traverse is used to mount probes for data acquisition. A pitot-static tube is mounted at the entrance of the test section to acquire total and static pressures which are used to determine the flow speed and act as the reference pressure for calculations of the pressure coefficient (C_p).

B. Airfoil Models

Two NACA 0012 airfoils are used for this project. The airfoil models were constructed at The University of Arizona using primarily polyoxymethylene (i.e., Delrin) along with an aluminum trailing edge and steel spar at $1/4$ chord. The models have a chord length of $c = 0.3048$ m (12 in) and a span of $b = 0.8636$ m (36 in). One model serves as the disturbance generator while the other functions as the target. Both models contain 64 static pressure ports. Forty taps are aligned at mid span while the others are evenly distributed at $1/4$ and $3/4$ span to evaluate 3D behavior. Both airfoils are mounted vertically in the wind tunnel and one end of the airfoil uses a foam spacer to eliminate gaps with the wind tunnel ceiling. Two plugs at the top and bottom hold the airfoil spar in place and two dowel pins, one on each plug, ensure that the airfoil does not rotate independently thus eliminating twist. The plugs can be rotated to adjust the angle of attack with uncertainty less than 0.25° . For VBI studies, the airfoils are separated by 6 chord lengths as sketched in Figure 8. All experiments are performed at a chord-based Reynolds number of 740,000 (40 m/s).

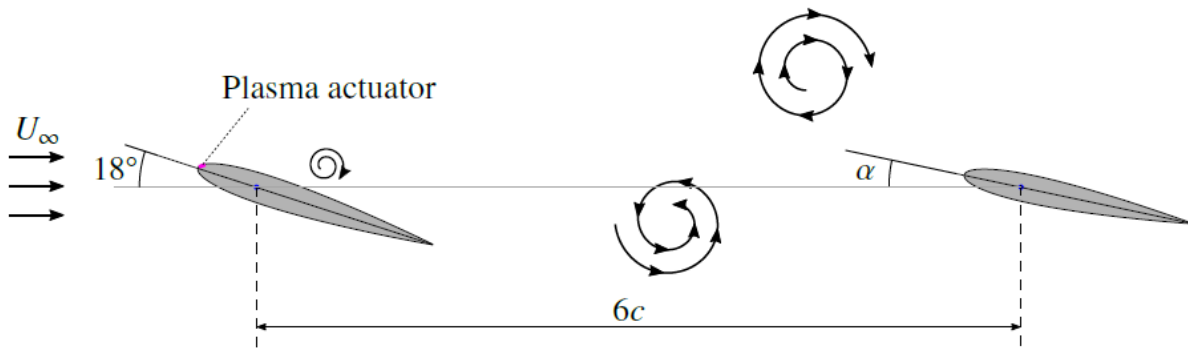


Figure 8: Sketch of experimental setup for studies of VBI showing disturbance (left) and target airfoil.

C. Instrumentation

A Scanivalve E-RAD400 is used to perform pressure measurements. This system consists of a ZOC33/64Px electronic pressure scanning module used in conjunction with a RADBASE4000 base unit with a RAD 3200 A/D converter. The pressure range of the selected module is $p_{max} = 6,895$ Pa (1.0 psi). The resolution of the system is given as $\pm 0.12\%$ of the full-scale reading, or $p_{resolution} = 8.32$ Pa (0.0012 psi). The freestream dynamic pressure at $U_\infty = 40$ m/s is $q = 980$ Pa (0.142 psi), meaning that resolution of the system is 0.8% of dynamic pressure. Fifty pressure data samples are collected in 32 s ($f_{sample} = 1.56$ Hz). The resulting values are used to compute the static C_p distribution over the airfoil surface having a statistical uncertainty of C_p of at most 2% with a confidence interval of 95%. For VBI studies, time-resolved pressure measurements are acquired at 625 Hz and phase-averaged over at least 100 cycles. Each pressure tap is connected to the sensing unit using 1.2 m vinyl tubing having a diameter of 0.0625 in. Corrections for the tubing length are implemented according to Bergh and Tijdeman (1965).

A LaVision 2D PIV system (DaVis 8.3.0) is used to obtain spatially resolved velocity data. Submicron DEHS seed particles are injected into the tunnel using a LaVision aerosol generator. A double-pulsed 200 mJ Quantel Evergreen laser is used in conjunction with spherical and cylindrical lenses to form a light sheet for the PIV measurements. The laser repetition rate is nominally 15 Hz. The time separation between laser pulses used for particle scattering is set according to the flow velocity, camera magnification, and correlation window size. Images corresponding to the pulses from each laser head are acquired by 16 bit 5.5 megapixel LaVision Imager sCMOS cameras incorporating Nikon Nikkor 50 mm f 1.2 lenses and narrow bandpass optical filters. For each image pair, sub-regions are cross-correlated using decreasing window size (64^2 – 32^2 pixel²) multi-pass processing with 50% overlap. The resulting velocity fields are post-processed to remove vectors with correlation peak ratio less than 1.5 and a correlation coefficient below 0.5. Removed vectors are replaced using an interpolation scheme based on the average of

neighboring vectors. A 3×3 Gaussian smoothing filter is also applied to the calculated velocity fields. The spatial resolution of the PIV is at or better than 3.62 mm (1.2% of chord) in all cases. Time-averaged data are produced from 500 instantaneous samples resulting in an uncertainty on velocity of 5.62% or less of freestream using a 95% confidence interval. Phase-averaged data are composed of 250 samples rendering uncertainties less than 1.5% of freestream using a 95% confidence interval.

Constant temperature anemometry (CTA) is performed using a Dantec Streamware Pro system with 55P01 probes and 55H21 supports. Probes are positioned in the wake of the disturbance airfoil at $x/c=6$ (see Figure 8) at various spanwise locations. The sampling rate of the hot wire measurements is 10 kHz for 200,000 total samples resulting in a total measurement duration of 20 s. The power spectrum density (PSD) is calculated using 60 blocks each containing 8192 samples. A Hanning window is applied to each block and an overlap of 50% is employed. Three probes are acquired simultaneously and the magnitude squared coherence is employed to evaluate the two-dimensionality in the wake of the disturbance generator using the same parameters as the PSD.

D. DBD Plasma Actuators

DBD plasma actuators are composed of two copper tape electrodes separated by Kapton tape dielectric arranged in an asymmetric fashion (Figure 9). The actuator is placed on the airfoil leading edge and covers most of the span except for regions near the tunnel sidewalls where electrical connections are made. The actuator is arranged such that the boundary layer forming from the stagnation line sees the plasma discharge before encountering discontinuities generated by the copper tape (i.e. the discharge is directed upstream). The covered ground electrode is 12.7 mm (1/2 in.) wide and the exposed high-voltage electrode is 6.35 mm (1/4 in.) wide. Each electrode has a thickness of 0.09 mm (3.5 mil). The dielectric barrier is composed of 2 layers of 0.76 mm (3 mil) Kapton tape with a dielectric strength of 10 kV. Each layer of Kapton tape has a 0.04 mm (1.5 mil) layer of silicone adhesive such that the actual Kapton thickness for each tape layer is only 0.04 mm (1.5 mil). The total thicknesses of the dielectric and the device as a whole are 0.15 mm (3 mil) and 0.30 mm (6 mil), respectively. The actuator construction was optimized based on previous work in airfoil separation control using ns-DBD plasma actuators (Little et al. 2012).

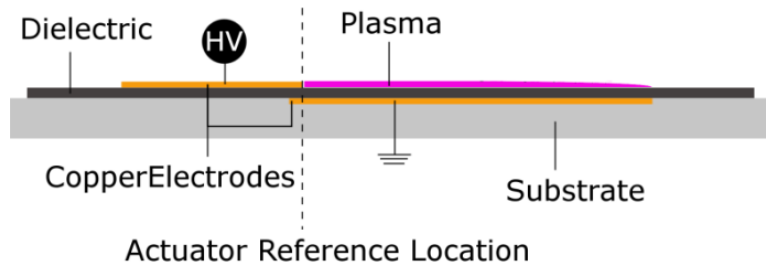


Figure 9: Typical asymmetric dielectric barrier discharge geometry (Dawson and Little 2013).

High voltage nanosecond pulses are produced using a pulse generator designed and built by the Ohio State University (OSU) Nonequilibrium Thermodynamics Laboratory (NETL). The pulser is magnetic compression type, capable of both positive and negative polarity outputs with bandwidth of 3 kHz. Only positive polarity pulses are studied here. Pulse voltage is controlled by a 5 kW Sorenson dc power supply capable of 0-700 V output. Input signals are generated by a Tektronix AF6310 function generator. A Tektronix P6015A high voltage probe and custom current probe are used in conjunction with a Tektronix TDS 2024C oscilloscope. Pulse voltage is measured at the output of the generator while current is measured between the encapsulated electrode and ground. A pair of 40 cm transmission cables connect the pulser to the DBD load.

Representative voltage and current traces on an 85.8 cm (33.78 in.) ns-DBD plasma actuator are shown in Figure 10a (linear dimension is into the page in Figure 9). The ns-DBD pulse width is ~ 200 ns and reaches a peak voltage of ~ 7.5 kV with max current of ~ 0.7 A/cm. Figure 10b plots instantaneous power and energy coupled to the load at these conditions. Steady-state energy of ~ 0.35 mJ/cm is realized

approximately 150 ns after the beginning of the pulse. The energy is calculated by integrating the absolute value of the product of voltage and current (Dawson and Little 2013). Note that pulse energy best characterizes the amplitude and typical values are on the order of 1 mJ/cm or less in flow control applications. Due to the length of the actuator, the peak power is only about 0.06 kW/cm. The pulse rise and fall time is nearly $t = 100$ ns, which is somewhat longer than previous experiments with this pulse generator. Also note that the pulse energy per unit length is slightly lower compared to previous work (Little et al. 2012). This is due to the relatively large size of the actuator. It will later be shown that even this small energy is sufficient for exciting the flow.

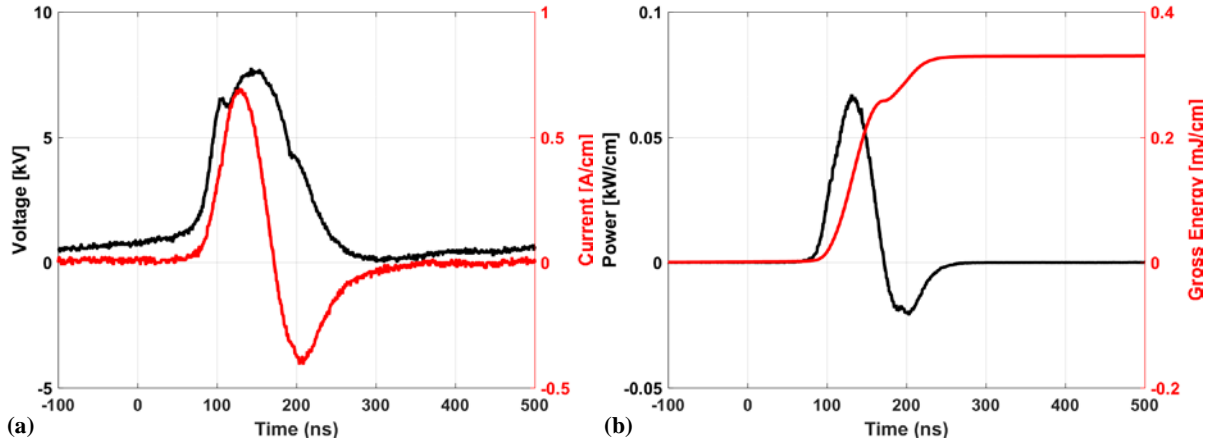


Figure 10: Sample traces of (a) Voltage and Current and (b) Instantaneous Power and Energy for a 76.5-cm-long (30 in.) ns-DBD actuator.

The short duration pulses produced by ns-DBDs generate weak levels of momentum and are deemed inconsequential in moderately high speed ($M > 0.1$) flow control demonstrations. Instead, the control authority stems from rapid localized heating of the near surface gas (Joule heating). The signature of this heating is a compression wave shown in Figure 11. Figure 11a presents schlieren images visualized along the major axis of the discharge similar to the viewing angle in Figure 9. The cylindrical wavefront originates from the electrode interface (actuator reference location in Figure 9) while the quasi-planar wave forms from spreading of the discharge on the dielectric surface. The speed of the compression waves reaches sonic after only a short distance from the surface, but is believed to be substantially greater very near the discharge (Roupassov et al. 2009; Takashima et al. 2011). Figure 11b shows schlieren images viewed along the minor axis of the discharge. It is now apparent that the cylindrical and quasi-planar waves are also composed of individual spherical wave fronts. These originate from localized hot spots in the discharge that remain stationary from pulse to pulse for a given actuator. Measurements of discharge overheat near the surface are quite challenging due to the spatial and temporal scales involved, but values as high as 350-400K have been reported (Roupassov et al. 2009; Takashima et al. 2011). It should be noted that heating effects from ac-DBDs have been disregarded in various studies (Enloe et al. 2004; Jukes et al. 2006; Sung et al. 2006).

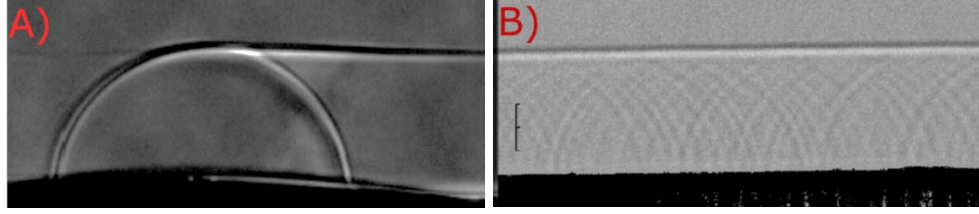


Figure 11: Sample phase averaged schlieren images of ns-DBD compression waves along the major (a) and minor (b) axis of the discharge. The length scale (bottom left of image b) shows 2mm (Dawson and Little 2013).

VI. Results

A. Airfoil Characterization

The airfoil models are characterized at a freestream velocity of 40 m/s corresponding to a Reynolds number of 740,000. The experimentally measured sectional lift coefficient is compared with XFLR5 calculations in Figure 12. The sectional lift coefficient for both models matches well with thin airfoil theory in the linear region of the curve. Predictions from XFLR5 are also in good agreement with the experiment up to an angle of attack of 12° . There are some slight and not unexpected differences in post-stall C_l for the two models between 12.5° and 15.5° . Beyond this ($16-20^\circ$), the experimental data sets again match well with the disturbance airfoil showing slightly larger lift. AFC is applied to the disturbance airfoil at 18° in the majority of the following data sets.

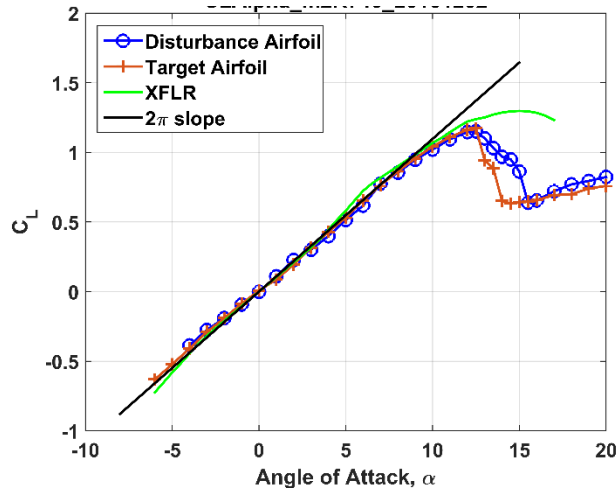


Figure 12: Lift coefficient vs angle of attack at $Re = 740,000$ for the disturbance and target airfoil compared to thin airfoil theory and XFLR5.

The selection of this angle is motivated, in part, by observations in the literature. Figure 13 shows a description of possible flow patterns over a NACA 0012 airfoil for a variety of studies (both computations and experiments). The existing work is shown as a red dot. This value falls near the high Re end of the “low-frequency regime.” The natural low frequency unsteadiness documented by Wu et al. (1998) and others indicates that the flow is particularly sensitive in this Re -AoA space and can develop low frequency shedding behavior presumably due to all manner of disturbances. The development of this low frequency behavior is presumably due to coupling between the shear layer and wake instabilities. The existence of a natural low frequency shedding regime is promising for this research. Efficient use of AFC relies on the manipulation of natural flow instabilities. The fact that these instabilities are excited even in baseline conditions implies they should be quite amenable to forcing. In addition, this figure also provides

motivation for the practical relevance of this work. Clearly, airfoils (both NACA 0012 and others) generate low frequency vortex shedding over a large parameter space. This parameter space may be encountered in various applications that include upstream geometries whose wake interacts with downstream components (e.g., rotorcraft, wind turbines, turbomachinery). Until now, a controlled method of producing such VBIs over a wide frequency range has not been explored.

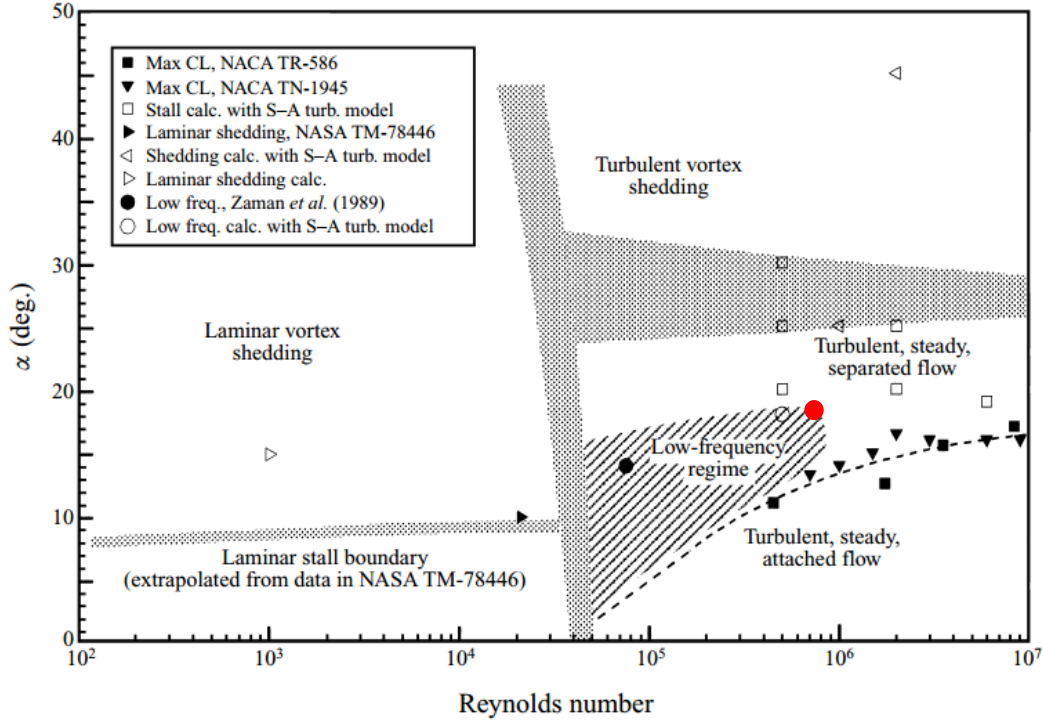


Figure 13: Possible regimes of flow patterns over a NACA-0012 airfoil at post-stall angles of attack versus Reynolds number. All data are taken from experiment unless noted. Shaded regions denote tentative approximate boundaries (Wu et al. 1998). The existing work is shown as a red dot.

B. Boundary Layer Separation and Wake Control

a. Test Conditions

Control of boundary layer separation and the wake of a NACA 0012 airfoil is presented for $Re = 740,000$ (40 m/s) with a post-stall angle of attack of 18° at atmospheric temperature and pressure. For all measurements, data are acquired by establishing a separated flow baseline condition and then energizing the ns-DBD plasma actuator. This work can be compared to published results on a NASA EET (Little et al. 2012) and NACA 0015 (Rethmel et al. 2011) airfoil.

b. Pressure Measurements

To select the optimum placement of the ns-DBD plasma actuator on the leading edge of the airfoil, C_p measurements were taken at 1 mm, 2 mm, 3 mm, 4.5 mm, and 6 mm. The actuator locations are referenced as an arc length from the leading edge ($x/c = 0$) to the plasma actuator. The actuator interface is on the suction surface in all cases (see Figure 9) and the plasma forms in the upstream direction. Note that installation of the actuator prevents the use of all pressure taps at the leading edge. On the pressure side, seven mid-span and two 3D pressure taps are lost while on the suction side, five mid-span and two 3D pressure taps are lost. Thus, the pressure tap nearest the leading edge with reliable data on the suction side of the airfoil corresponds to $x/c = 0.09$. For each location, frequency sweeps are conducted between $F^+ =$

0.08 – 7.62 ($f_f = 10 \text{ Hz} - 1 \text{ kHz}$) at angles of 16° , 17° , 18° , and 19° . The 3 mm actuator location yielded best results at 18° suggesting actuation is occurring near the receptivity region and offers the most favorable conditions for this study. To illustrate this, frequency sweeps for the 3 mm actuator location are shown at two angles of attack in Figure 14. At 18° , a forcing frequency of $F^+ \approx 1.14$ corresponds to the lowest C_p at $x/c = 0.09$ indicating the best condition for separation control. The same experiment is also shown for 16° to emphasize the fundamental differences in the flow response at these two conditions. In the low AoA case, the C_p value decreases significantly as forcing frequency is raised. After $F^+ \approx 0.5$, the C_p value is essentially constant. The behavior indicates that AFC is acting as an active boundary layer trip and this has also been observed for a NASA EET airfoil (Little et al. 2012). Both observations are consistent with Figure 13. At 16° , increasing Re to 10,000,000 enters the turbulent, steady attached flow regime and this is approximated by the active boundary layer trip employed here. At 18° , turbulent steady attached flow is not observed and the active trip scenario does not occur.

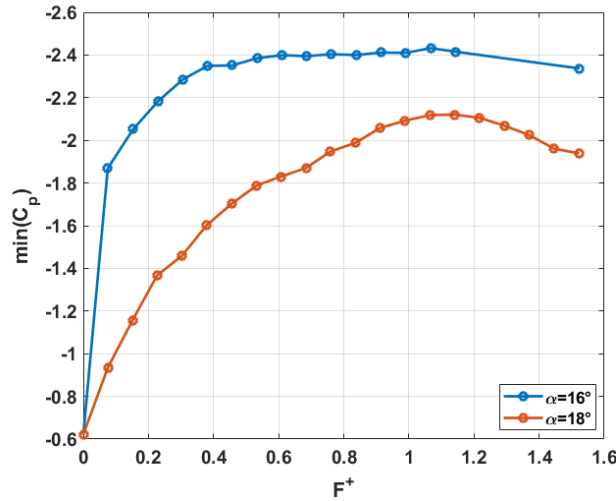


Figure 14: Suction side C_p at $x/c = 0.09$ vs. dimensionless forcing frequency, F^+ , for NACA 0012 airfoil at $Re = 740,000$ and $\alpha = 18^\circ$.

Figure 15a-c show representative C_p plots with mid-span and 3D pressure tap distributions. Note the missing data near the leading edge due to the installation of the actuator. Variations between the mid-span and 3D values are negligible, and as a result, the flow is presumed 2D over the central $\frac{1}{2}$ span of the airfoil even for AFC cases. Select frequencies shown in Figure 15a-c represent cases chosen for closer investigation with PIV. The baseline flow is characterized by a near-zero pressure gradient along the suction side of the airfoil indicating deep stall as expected. All forcing frequencies show an improvement over the baseline and it is clear that the best case for separation control is $F^+ \approx 1.14$ ($f_f = 150 \text{ Hz}$). Note that forcing at $F^+ \approx 1.52$ ($f_f = 200 \text{ Hz}$) is also quite successful, but reaches a slightly higher C_p value (Figure 15d). While it is not clear from pressure distributions, the cases presented here indicate different forcing regimes and will be discussed in detail in the following sections.

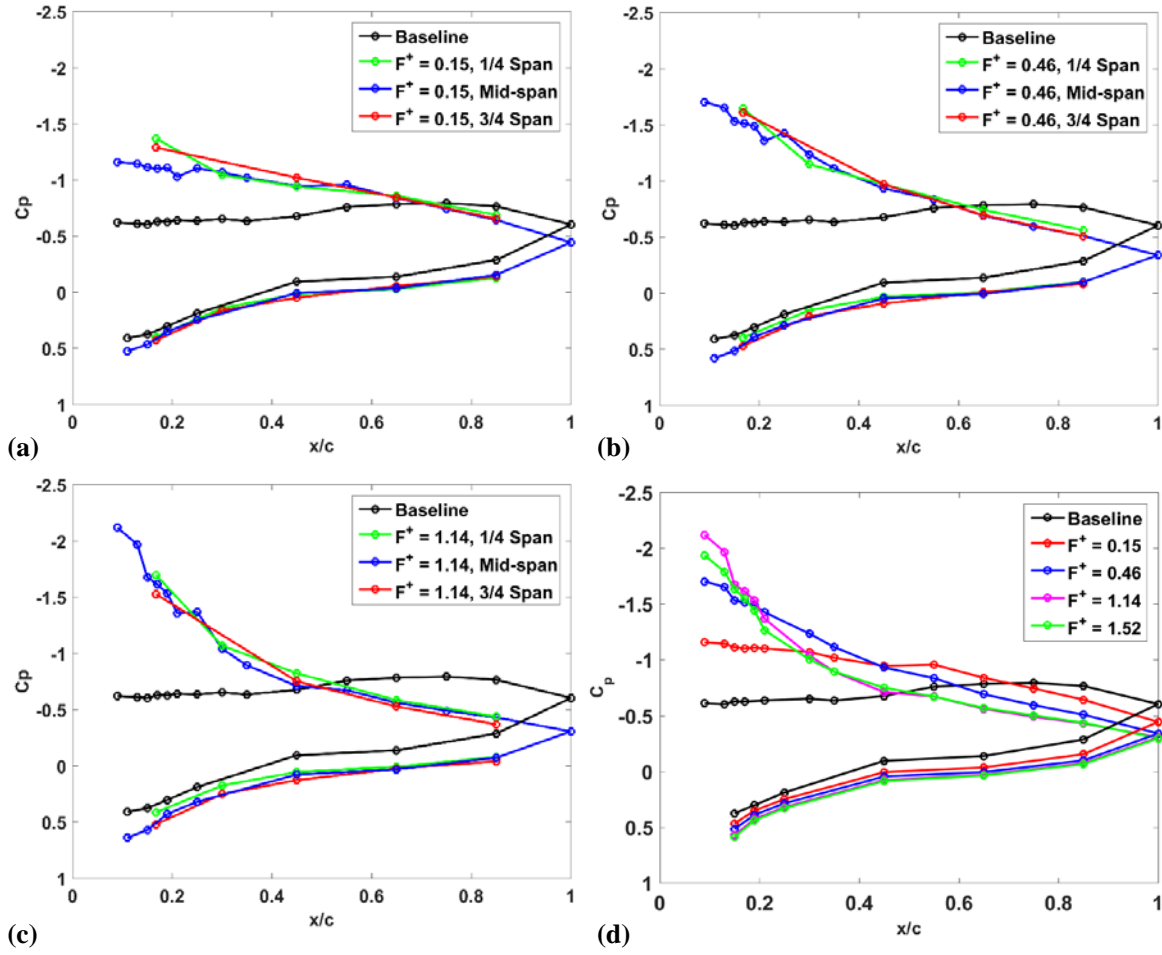


Figure 15: (a) Mid-span and 3D C_p distribution for $F^+ \approx 0.15$ (20 Hz), (b) $F^+ \approx 0.46$ (60 Hz), (c) $F^+ \approx 1.14$ (150 Hz) and (d) C_p distribution for select control cases.

c. PIV Results

2D PIV is used to map the flow field from the leading edge of the disturbance airfoil to approximately 4.5 chord-lengths downstream in the wake. One camera is used to capture the flow over the airfoil surface with a mask chosen to omit the regions contaminated by the wall plug. The wake from $x/c=1$ to 4.5 is captured in a subsequent and identical test run using two cameras side-by-side. The data are processed and mapped to provide a quantitative visualization of the flow. This configuration shows a reasonably large field of view for studying the ns-DBD's ability to control separation over the airfoil as well as to produce coherent structures in the wake. PIV is measured for the baseline flow and various forcing cases. Results presented here show the baseline flow, a low frequency case ($F^+ \approx 0.15$ (20 Hz)) which possesses some characteristics of an impulse response, a case showing very coherent behavior in the wake ($F^+ \approx 0.46$ (60 Hz)) and the best forcing frequency for separation control ($F^+ \approx 1.14$ (150 Hz)).

Figure 16 shows a comparison of the dimensionless time-averaged streamwise velocity for the baseline and each forcing case under consideration. Both contours of streamwise velocity and corresponding velocity profiles at $x/c = 2$ are provided. It is clear that the airfoil is fully-stalled for the baseline case. An increase in forcing frequency shows a progressive decrease in flow separation which is consistent with the C_p data in Figure 14. The associated velocity profiles at $x/c = 2$ show more quantitatively that the momentum deficit in the wake is being reduced as expected.

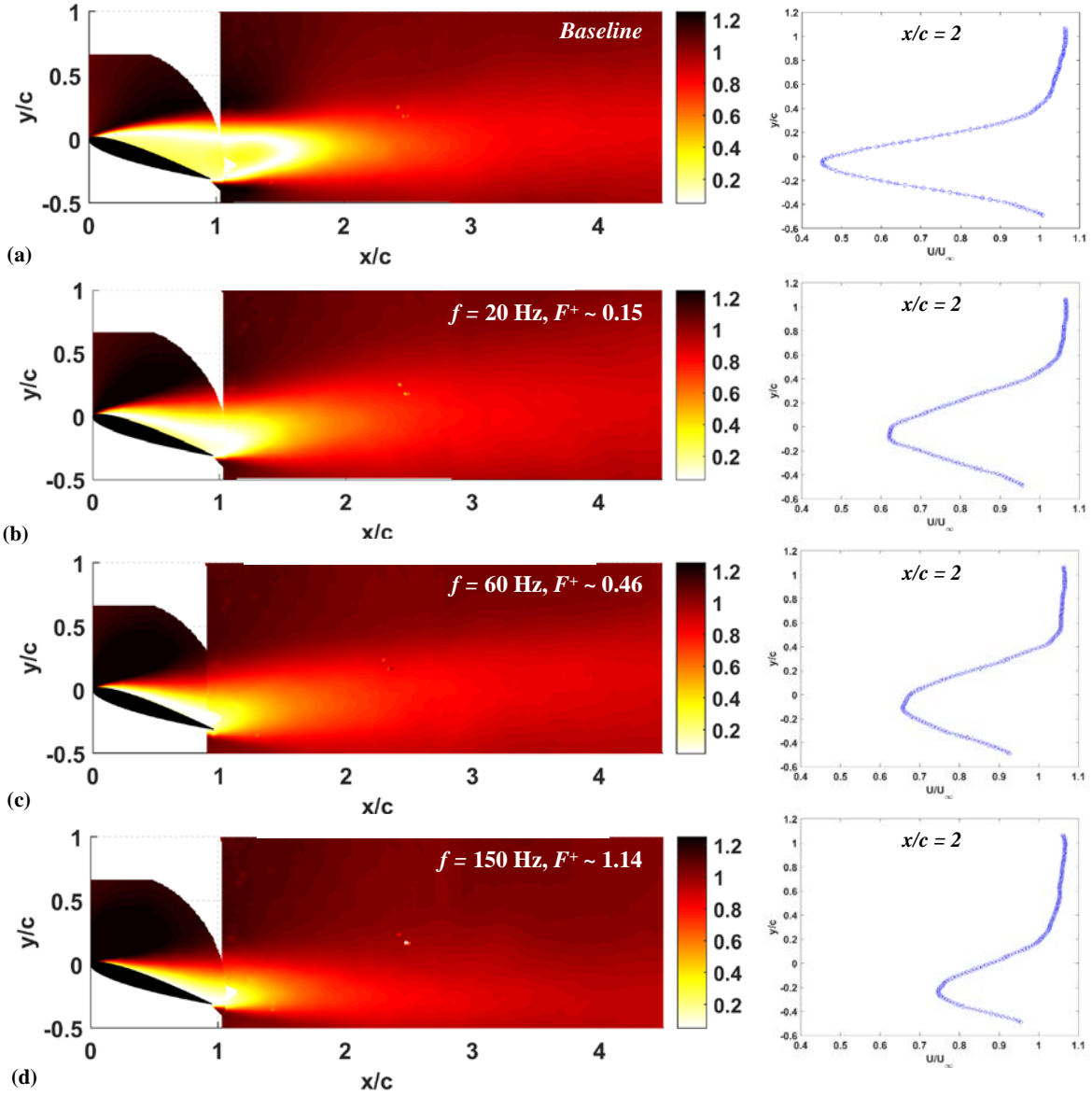


Figure 16: Plots of time-averaged dimensionless streamwise velocity at $Re = 740,000$, $\alpha = 18^\circ$ (a) Baseline case (no control) and ns-DBD forcing at (b) $F^+ \approx 0.15$ ($f = 20$ Hz) (c) $F^+ \approx 0.46$ ($f = 60$ Hz) and (d) $F^+ \approx 1.14$ ($f = 150$ Hz).

Phase-averaged transverse velocity fluctuations and vorticity in Figure 17 and Figure 18 provide insight into the actuator's ability to produce disturbances in the wake. In the former, a pair of positive and negative regions represents flow structure. Four equally distributed phases are shown corresponding to the three forcing cases in Figure 16. The first phase (top row) is acquired just after the high voltage pulse is applied. The relative timing of the phases is not important for the $F^+ = 0.46$ (60 Hz) and $F^+ = 1.14$ (150 Hz) cases since the flow response is sinusoidal. However, forcing in the low frequency case $F^+ = 0.15$ (20 Hz) behaves like a repetitive impulse. Shortly after the actuator is fired, a large structure develops and propagates over the airfoil and into the wake. The length scale of this structure is approximately the airfoil chord. After the disturbance propagates into the wake, a modest positive velocity fluctuation is observed over the airfoil seemingly due to the reestablishment of the baseline state. The fact that a nonzero fluctuating

velocity exists over the airfoil after the disturbance propagates downstream implies that the baseline state is not quite reestablished before initiation of the next plasma pulse. The transient behavior associated with single pulse forcing is explored in Section VI.C. The rotation of the dominant disturbance is not necessarily clear in the low frequency ($F^+ = 0.15$ (20 Hz)) case of Figure 17. Coupling this with the vorticity in Figure 18, it is now apparent that the counter-clockwise vorticity shed from the pressure side is actually more dominant and in line to impinge upon the downstream airfoil. The clockwise rotating structure that is shed from the suction surface appears substantially weaker. It is proposed and will later be shown that VBI produced by relatively low frequency AFC ($F^+ < 0.15$ (20 Hz)) in this particular configuration is dominated by a single counter clockwise vortex impinging on the target airfoil.

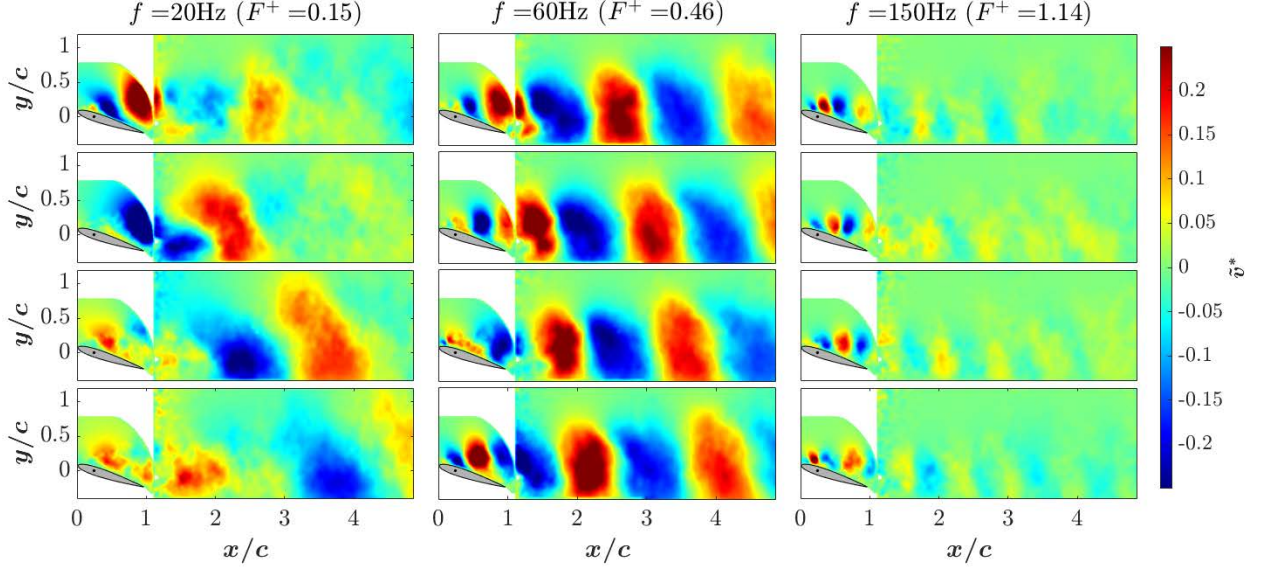


Figure 17: Phase-averaged transverse velocity fluctuations for ns-DBD forcing at $F^+ \approx 0.15$ (20 Hz), $F^+ \approx 0.46$ (60 Hz), $F^+ \approx 1.14$ (150 Hz).

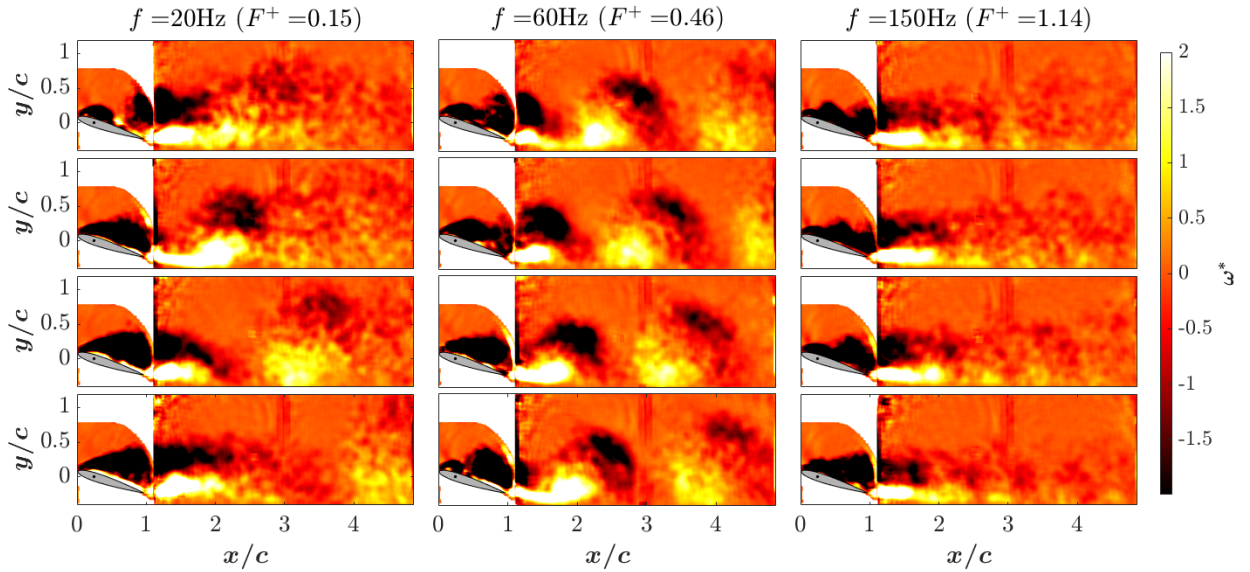


Figure 18: Phase-averaged vorticity for ns-DBD forcing at $F^+ \approx 0.15$ (20 Hz), $F^+ \approx 0.46$ (60 Hz), $F^+ \approx 1.14$ (150 Hz). Note that the unphysical vertical lines near $x/c = 3$ in the vorticity fields are due to stitching of the two camera images.

The phase-averaged transverse velocity fluctuations for $F^+ = 0.46$ (60 Hz) in Figure 17 are strikingly different than the low frequency case ($F^+ = 0.15$ (20 Hz)). A very organized pattern of positive and negative fluctuations is now visible in the wake throughout the entire field of view for all phases. The amplitude of these fluctuations is somewhat stronger near the airfoil, but still approximately 25% of the freestream at the downstream end of the domain. It is insightful to note that the both amplitude and size of the dominant disturbance in the low frequency case ($F^+ = 0.15$ (20 Hz)) is quite similar to the first phase of this case ($F^+ = 0.46$ (60 Hz)). However, consideration of the vorticity fields reveals that both positive and negative vortex pairs are now present.

The phased-averaged transverse velocity fluctuations $F^+ = 1.14$ (150 Hz) in the wake are comparatively much weaker than the two lower frequency cases. However, organization over the airfoil chord is very apparent as expected for successful separation control. These coherent structures dominate the flow over the airfoil and their number and size is consistent with forcing at $F^+ \approx 1.14$. It is well-established that these structures are effective for entraining freestream momentum and reattaching separated flows (Greenblatt and Wygnanski 2000). This behavior is washed out in the vorticity field highlighting utility of the less commonly transverse velocity data in Figure 17. From Figure 14, ns-DBD control at $F^+ \approx 1.14$ corresponds to the minimum C_p nearest the leading edge, translating to the best case for separation control. Forcing at $F^+ \approx 1.14$ creates a strong suction peak near the leading edge and reattaches the flow in the mean over nearly the entire suction surface (see Figure 15). Consistent with previous studies, the control mechanism in this case is not due to laminar to turbulent transition, but rather due to the excitation of flow instabilities through ns-DBD produced thermal perturbations. Further discussion of the physics and scaling of ns-DBD plasma actuators and thermal energy deposition for AFC in general can be found in Little (2018).

d. Constant Temperature Anemometry

Finally, constant temperature (hot-wire) anemometry is employed to quantify the spectra and coherence in the excited wake. Data are collected over a range of forcing cases from $F^+ = 0.08 - 1.22$ (10 – 160 Hz) in increments of $\Delta F^+ = 0.08$ (10 Hz). To coincide with the PIV measurements, focus is initially placed on $F^+ = 0.15, 0.46$, and 1.14 (20, 60, and 150 Hz respectively). All CTA data is acquired at $x/c = 6$ with varying spanwise locations.

Figure 19a shows PSD at mid-span for the baseline and three forcing cases. The transverse location of all CTA data is at $1/4$ chord. All cases present a well-developed inertial subrange over more than a decade of St . The frequency at which the inertial subrange becomes apparent is not appreciably different for the various cases. The baseline is absent a clear spectral peak as expected and the same can be said of the highest forcing frequency case ($F^+ = 1.14$ (150 Hz)). Recall that this forcing frequency resulted in the best performance in terms of separation control. PIV data indicate a very robust pattern over the airfoil (see Figure 17), but this behavior diminishes quickly in the wake such that the forcing signal is no longer visible above the background turbulence at $x/c = 6$. Note that the PSD magnitude at high frequency is slightly reduced in this case. Forcing at $F^+ = 0.46$ (60 Hz) results in a single dominant peak in the spectrum while lower frequency forcing ($F^+ = 0.15$ (20 Hz)) contains a peak at the fundamental ($St = 0.15$ (20 Hz)) and two harmonics ($St = 0.3$ (40 Hz) and $St = 0.45$ (60 Hz)). All forcing cases have higher broadband PSD magnitude compared to the baseline below the onset of the inertial subrange ($St < 0.45$ (60 Hz)).

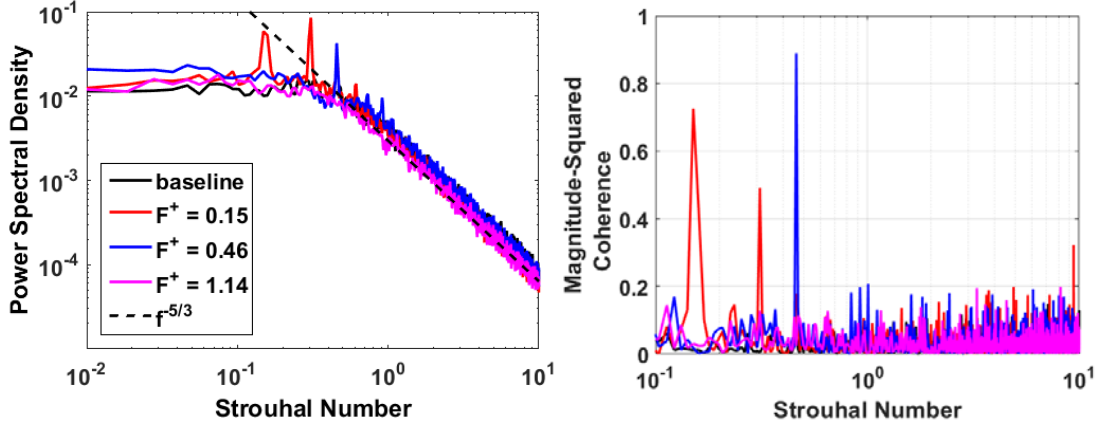


Figure 19: (a) Mid-span PSD and (b) coherence spectra across the central $\frac{1}{2}$ of the wake (1.5c) for select forcing frequencies at $x/c=6$.

Figure 19b shows the coherence between probes mounted at $\frac{1}{4}$ and $\frac{3}{4}$ span (separation of 1.5c). As with PSD, the baseline and high frequency case ($F^+=1.14$ (150 Hz)) expectedly show no clear peaks. Forcing at $F^+=0.46$ (60 Hz) results in very coherent behavior across the central 1.5c of the wake having a normalized value of approximately 0.9. In the low frequency case ($F^+=0.15$ (20 Hz)), the existence of multiple harmonics is apparent and consistent with the PSD. Overall, the PSD and coherence data in Figure 19 show that cases that excite the wake ($F^+ = 0.15$ (20 Hz) and $F^+ = 0.46$ (60 Hz)) not only do so, but do so in a very coherent fashion over the central $\frac{1}{2}$ span of the wind tunnel (1.5c). This observation is further strengthened by contour plots of PSD and coherence for the entire range of surveyed AFC frequencies (Figure 20). The dashed line is provided to emphasize a slope of one. Note that breaks in the high PSD and coherence levels are purely due to the chosen resolution in forcing frequency. Also, the PSD data are acquired at higher forcing frequency resolution. Essentially any frequency can be excited in the wake below the full onset of the inertial subrange ($St < 0.92$ (120 Hz)). This is most easily seen in the coherence plots (Figure 20b) since the PSD peaks are lost due to the chosen contour at high St . Forcing below $F^+=0.3$ (40 Hz) results in a peak at the fundamental as well as multiple harmonics and these frequencies are quite coherent across the central $\frac{1}{2}$ of the tunnel (1.5c). This observation is consistent with the subset shown in Figure 19 as well as PIV data in Figure 17. The existence of harmonics is consistent with a pulsed impulse-like disturbance lacking sinusoidal behavior. Between $0.3 < F^+ < 0.92$ ($40 < f < 120$ Hz), a single dominant frequency is produced in the wake (in agreement with Figure 17) and it is quite coherent across the central $\frac{1}{2}$ span (1.5c). Higher frequencies ($F^+ > 0.92$ (120 Hz)), while quite useful for separation control, do not produce significant disturbances at $x/c=6$ as previously discussed.

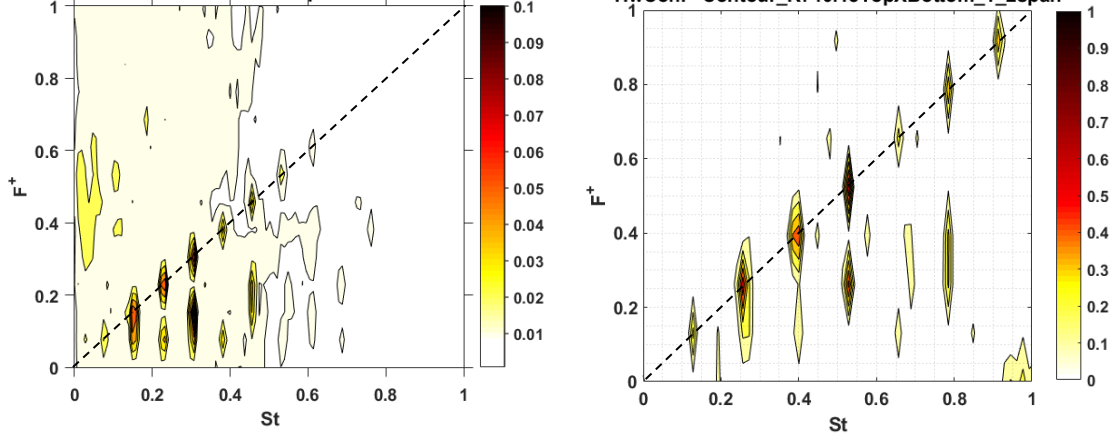


Figure 20: Contour plots of (a) PSD and (b) coherence spectra across the central $\frac{1}{2}$ of the wake (1.5c) for select forcing frequencies at $x/c=6$. The dashed line indicates a slope of one.

C. Transient Behavior

The transient behavior of the separated flow in response to a single pulse of ns-DBD plasma actuation is examined at various convective times after discharge initiation. Such studies of transient separation control have been undertaken using a variety of fluidic actuators (Amitay and Glezer 2002; Darabi and Wygnanski 2004b; Darabi and Wygnanski 2004a; Amitay and Glezer 2006; Mathis et al. 2007; Mathis et al. 2009; Williams et al. 2009; Brzozowski et al. 2010; Albrecht et al. 2015), but this is mostly unexplored with thermal energy deposition actuators such as ns-DBDs. While the transient behavior is of scientific interest, the focus here is also on characterizing the effect of forcing amplitude as it pertains to the AFC-generated disturbance. Essentially, this section examines the mechanisms by which a single disturbance is generated resulting in an isolated encounter with the target airfoil. Once again, the vortex shed from the pressure side is actually more relevant for VBI in the current setup, but this data has utility for other VBI orientations (e.g. airfoils offset in the transverse direction).

Figure 21 shows the vorticity field at various convective times. The baseline flow is also included for reference. Shortly after the actuation pulse at $t/T_{conv} = 0$, the shear layer is severed at the leading edge ($t/T_{conv} = 0.2$). At the location of severance, a clockwise rotating vortex is created and sheds from the leading edge. The freestream flow carries this structure downstream as seen in subsequent time delays. This shear layer vortex expands in diameter and weakens with advection over the chord. The vortex is transported to the wake and out of the field of view. Another structure is observed near the leading edge of the airfoil surface just after the shear layer is severed. This second vortex grows over the suction surface of the airfoil until the separated shear layer is fully reformed ($t/T_{conv} = 10$). The ns-DBD actuation pulse is much shorter than the convective time scale ($T_{pulse}/T_{conv} = 2.4 \times 10^{-8}$) yet the flow remains at least partially attached for up to two convective times. These results are qualitatively similar to other transient separation control studies using fluidic actuators, where reattachment also persisted for several convective times (Brzozowski et al. 2010). It should be noted that the ns-DBD pulse duration, T_{pulse} is quantified purely based on electrical data (e.g. Figure 10). It is not clear how to specifically define the time-scale of the thermal disturbance, but the reported value is certainly an underestimate. Regardless, it is expected that ns-DBD plasma forcing occurs on a time scale that is substantially shorter than previously explored fluidic actuators including pulsed combustion jet actuation having ($T_{pulse}/T_{conv} = 0.05$) to which these results are comparable (Brzozowski et al. 2010). Despite this and in agreement with Brzozowski et al. (2010), the effect of this very short duration actuator pulse persists for up to 8-10 convective times. The transient separation due shedding of the second vortex occurs in a manner that is consistent with dynamic stall.

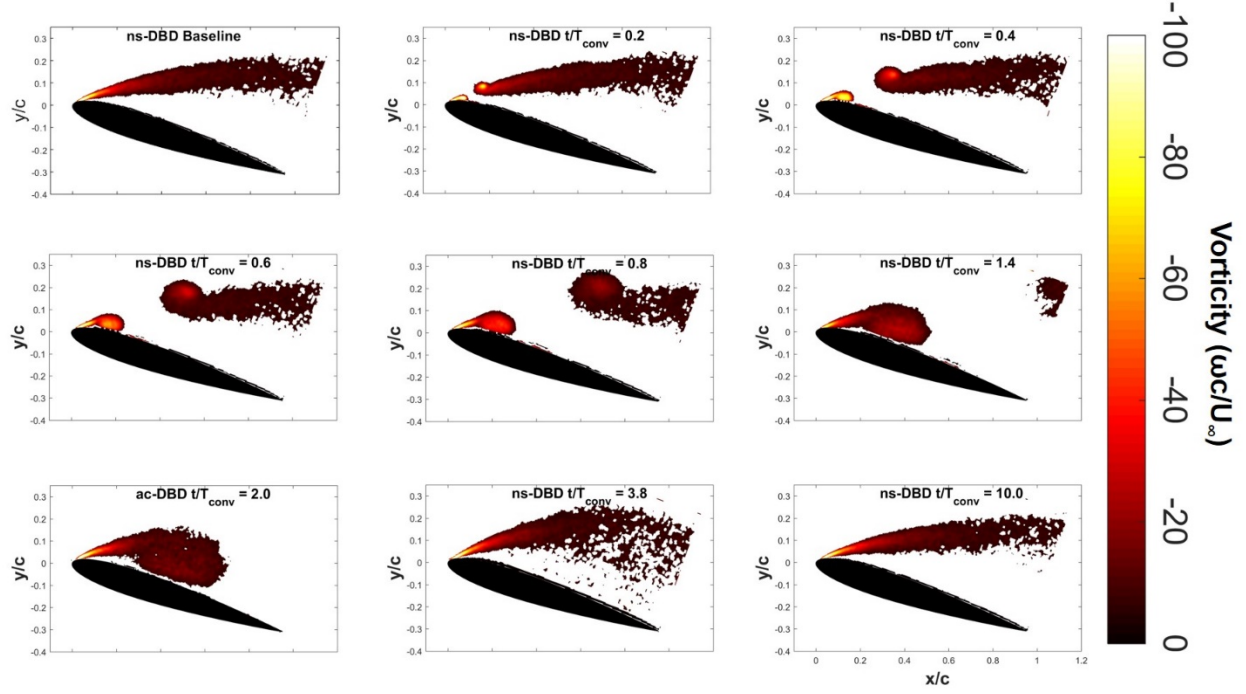


Figure 21: Response of the separated shear layer to ns-DBD forcing at various convective times.

A control volume analysis of the circulation is computed over the area shown in Figure 22a to provide a more quantitative comparison of the transient response to thermal energy deposition. This location is chosen to provide some context to the literature and data from Brzozowski et al. (2010) are included for reference. Those authors included a similar size window, but just downstream of the airfoil trailing edge such that vorticity flux from both the suction and pressure side was included. The latter had very little influence on the calculations hence the data from the current study should provide a reasonable comparison albeit slightly upstream. Figure 22b shows the variation of the normalized vorticity flux ($\frac{d\Gamma}{dt} = \int \bar{u}\bar{w} dA$) with convective time. Both curves indicate an initial slight increase and then decrease in circulation followed by another rise before relaxing back to zero. The first extremum ($t/T_{conv} < 1$) corresponds to the location at which the severed vortex passes the integration domain. The minimum value of $d\Gamma/dt$ near $t/T_{conv}=1$ is due to the severed region behind the vortex that is void of vorticity and this is apparently more extreme in the ns-DBD case. The maximum value of the quantity at $t/T_{conv} \approx 2$ is developed as the second vortex crossed the integration domain where again the ns-DBD value is larger in magnitude. Both data sets relax to zero after approximately three convective times. Figure 22c shows the change in circulation relative to the baseline flow, this is calculated by integrating $d\Gamma/dt$. The behavior is somewhat similar, but the ns-DBD case is now missing the slight peak just below one convective time. The negative peak at one convective time is nearly identical while the positive peak that follows is shifted to somewhat later convective times presumably due to discrepancies between the two studies. Both data sets decrease to the baseline value reaching it in nearly 10 convective times. The modest peak near $t/T_{conv}=7$ for the ns-DBD case is associated with the reformation of separated flow over the airfoil. This peak may be a by-product of insufficient spatial resolution in the PIV setup which is highlighted by the diffuse nature of the vorticity in the final stages of this process. As such, it is unclear if this is physically significant or just a representation of the uncertainty on the calculation. In addition to window location between the two studies, the Brzozowski et al. (2010) work is also for a different airfoil (NACA 4415) with a different actuator location ($x/c=0.2$) and type (pulsed combustion jet). Despite these significant differences, the global flow response is dramatically similar and the same results were found for momentum-based plasma forcing using ac-

DBDs (Durasiewicz et al. 2018). In summary, these findings show that the global response of the separated shear layer to single pulse actuation on stalled airfoils is dramatically consistent despite differences in geometry, control mechanism and actuator location. The very different physical processes employed in this work and others influence the local behavior. However, the similarity of the global effect is consistent with findings from Albrecht et al. (2015) who used various Lorentz forces actuator configurations albeit for much longer convective times (0.5). This further emphasizes that it is the flow field itself (in this case the flow instability) that governs the response and this is mostly independent of actuation. This further provides relevance for the AFC-based disturbance generation idea since the flow can be tuned to various frequencies which may arise from all manner of natural disturbances in the flight environment.

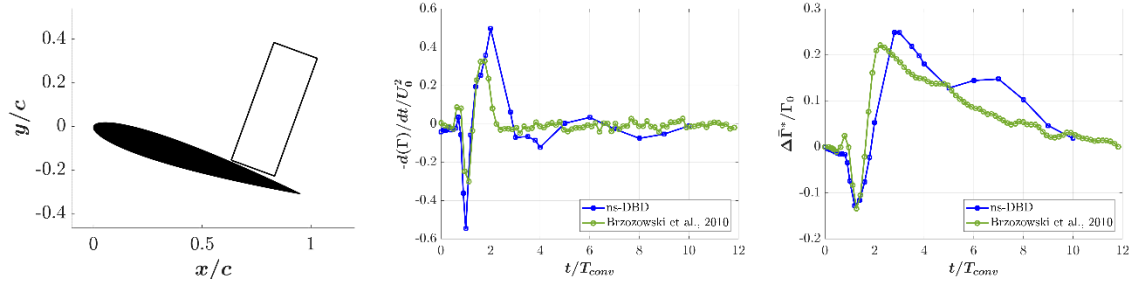


Figure 22: (a) Reference window used for calculations (b) Variation of normalized vorticity flux ($-\frac{d\Gamma}{dt} \frac{1}{U_\infty^2}$) with time (c) Variation of normalized circulation ($-\frac{\Delta\Gamma}{\Gamma_0}$) with time.

Finally, the influence of forcing amplitude on the AFC-generated disturbances is explored in Figure 23. Due to the model and actuator length, the available pulse energy variation is limited to a factor of three. It is clear from Figure 23 that variation of pulse energy in this range does not produce any obvious changes to the excited structure. Contours of both vorticity and transverse velocity are nearly identical. It seems plausible that a further increase in pulse amplitude would result in a change in the flow response. This has been observed in other experiments (Akins et al. 2015), but it is not attainable with the existing power supply. From a VBI perspective, the hardware and conditions examined here do not allow for a simple decoupling of the frequency and amplitude of AFC-based disturbances. However, a recent paper using a much smaller airfoil did show a variation in the transient flow response over an energy range of 0.006-0.6 mJ/cm (Komuro et al. 2018) and there is no reason that this could not be replicated for larger models provided a capable power supply is available.

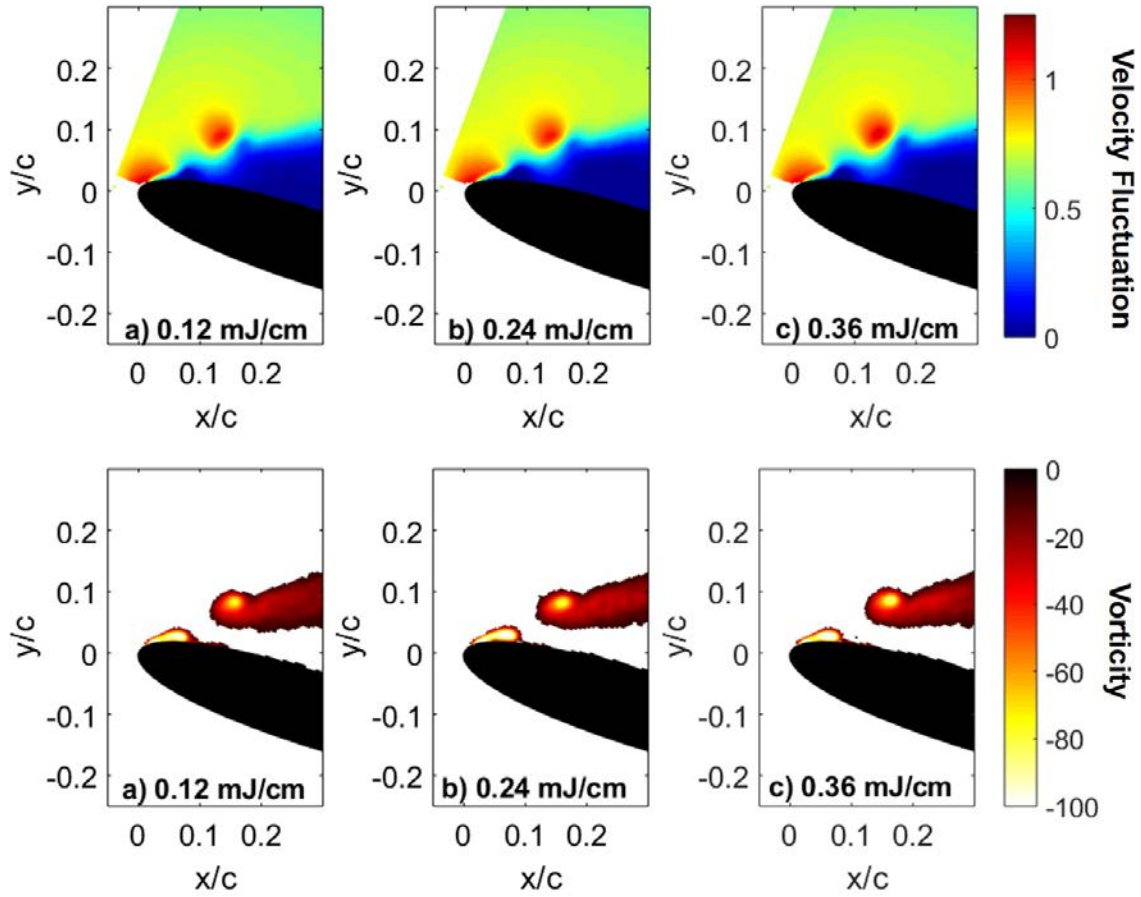


Figure 23: Normalized vorticity and transverse velocity for pulse energies of 0.12, 0.23 and 0.35 mJ/cm at $t/T_{conv} = 0.2$

D. Vortex Body Interaction

Having characterized the efficacy of ns-DBD plasma actuators for exciting the wake, a target airfoil is now immersed in the unsteady flow. At this time, only one disturbance/target airfoil combination has been employed (see Figure 8). As before, the ns-DBD plasma actuator is located near the leading edge of the disturbance airfoil and placed at a post-stall angle of 18° . Figure 24 shows the lift coefficient as a function of incidence for the airfoil in a uniform stream as well as in the baseline wake of the disturbance airfoil. Thin airfoil theory and XFLR5 data are also shown for reference. The slope of the curve is more mild in the wake case, but the most noticeable discrepancy is above 12° . The airfoil immersed in the baseline wake no longer stalls presumably due to accelerated boundary layer transition near the leading edge.

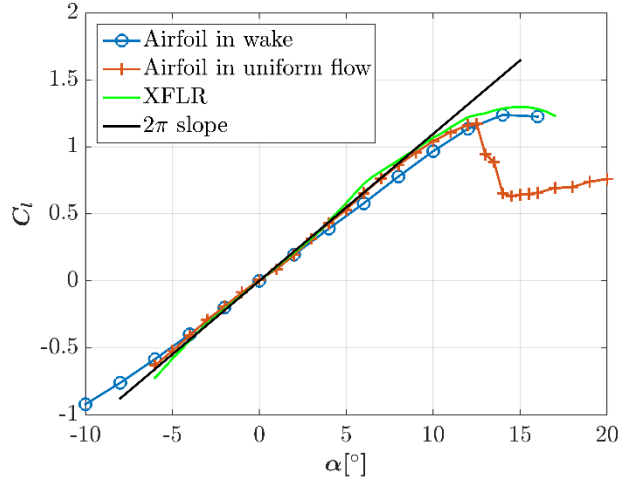


Figure 24: Lift coefficient vs angle of attack at $Re = 740,000$ for the target airfoil in a uniform stream and in the disturbance airfoil wake compared to thin airfoil theory and XFLR5.

Figure 25 shows the coefficient of lift and moment for the target airfoil immersed in the disturbance airfoil wake at four VBI forcing frequencies, $F^+ = 0.042$ (5 Hz), $F^+ = 0.169$ (20 Hz), $F^+ = 0.508$ (60 Hz) and $F^+ = 0.847$ (100 Hz). Note that the expression of F^+ in this section now employs the characteristic velocity in the wake at the airfoil location (36 m/s). Thus, the F^+ values, which represent different regimes of wake excitation, are increased by approximately 10% for the same dimensional forcing frequency compared to Section VI.B. Error bars indicate the maximum and minimum of the phase averaged signal for each angle of attack. The height of the error bars therefore serves as an indicator for the VBI strength, while stochastic effects of turbulence are removed through the phase averaging. It is first apparent that increasing the VBI frequency results in less variation in the integral coefficients. Also, the error bars are larger for higher incidence thus highlighting the importance of target loading on the VBI. It is also noted that average values for lift and moment coefficients are not drastically affected by the VBI and match those observed for the baseline case where the target airfoil is immersed in the wake.

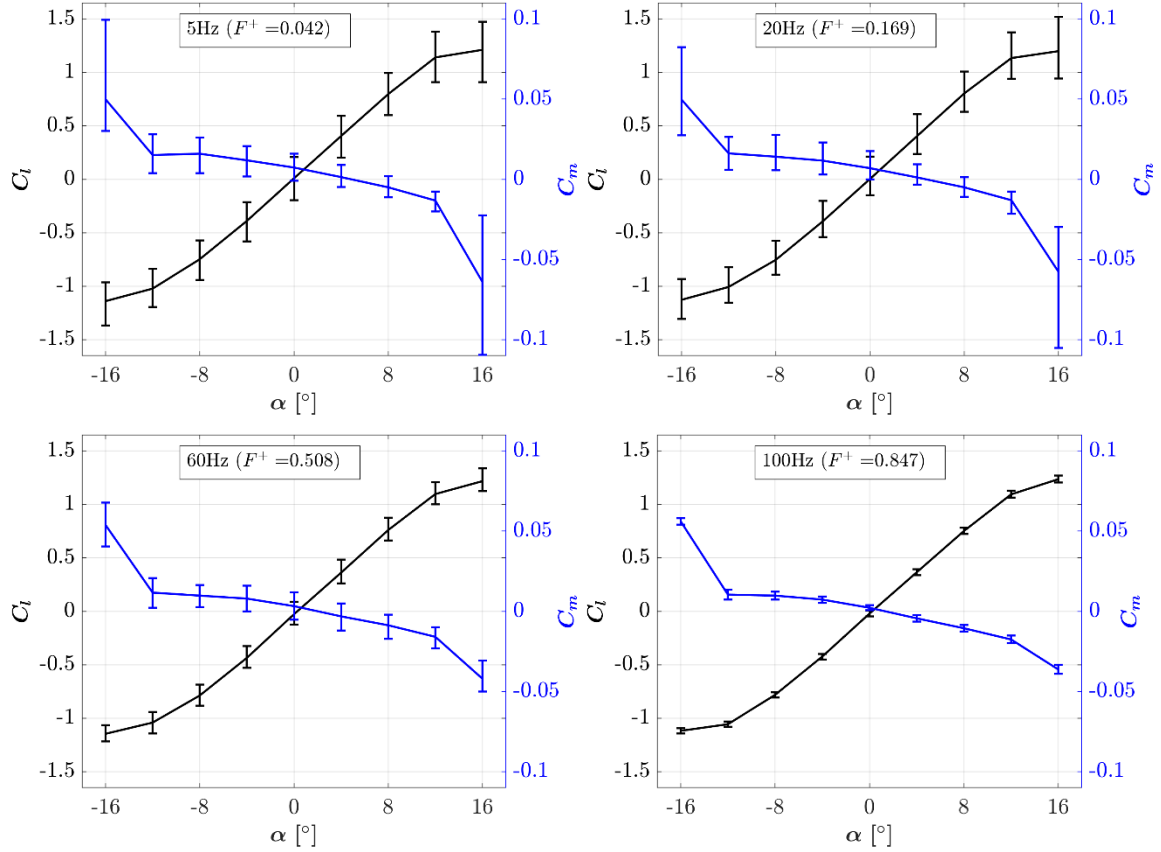


Figure 25: Coefficients of lift and moment as a function of actuation (VBI) frequency for the target airfoil immersed in the disturbance airfoil wake.

The variation of lift coefficient with respect to the phase of the disturbance is shown in Figure 26 for incidence angles of $\alpha = 0^\circ$ and $\alpha = 16^\circ$. The plots are generated by phase averaging the various VBI frequencies over a minimum of 100 cycles. Note that the relative phase between the various VBI frequencies is not meaningful. In the low frequency case ($F^+ = 0.042$ (5 Hz)) at an incidence angle of $\alpha = 0^\circ$, a strong symmetric disturbance in the lift coefficient is observed ranging between C_l of ± 0.2 after which a lower amplitude, but higher frequency oscillation is present. The ± 0.2 variation in C_l is due to VBI via an isolated encounter (see Section IV.B). This manifests in the spectrum of Figure 27 as a fundamental peak along with seven harmonics. The higher frequency lower amplitude oscillation in the phase averaged data appears as a peak near $St = 0.635$ (75 Hz). PSD of baseline C_l in Figure 27 reveals that for zero incidence, the target airfoil develops this same frequency. There is clearly some weak unsteady loading due to immersion of the target airfoil in the baseline wake. Also, this indicates that flow over the target airfoil has relaxed to its baseline state between VBI occurrences in the low frequency case supporting the idea of an isolated encounter. Increasing the VBI frequency to 20 Hz generates a more sinusoidal variation in C_l with excursions from the mean slightly biased toward the positive side. This behavior is not truly sinusoidal as can be seen in the C_l spectrum which contains the fundamental and 5 harmonics. VBI at 60 Hz is more sinusoidal with minor and nearly symmetric excursions from the mean. In this case, the fundamental and a single harmonic are observed in the spectrum. Finally, VBI at 100 Hz shows even less variation from the mean and is nearly sinusoidal as indicated by the single peak in the C_l spectrum.

Regarding the phase averaged C_l perturbations for $F^+ = 0.042$ (5 Hz), the VBI is governed by an increase in lift at first and a subsequent decrease in lift until a minimum is reached. Afterwards, the baseline flow is reestablished. This is in good agreement with the previous assumption that the VBI will be

dominated by one, counter clockwise rotating vortex in this case (see Section VI.B). As will be shown later, the vortex induces an angle of incidence on the target airfoil and therefore generating a lift perturbation. The C_l change implies a positive vertical velocity (upwash) at first, followed by a negative vertical velocity (downwash). This coincides with a counter-clockwise rotating vortex being convected downstream and interacting with the airfoil. This is expected for all isolated cases ($F^+ \leq 0.169$ (20 Hz)) in this configuration.

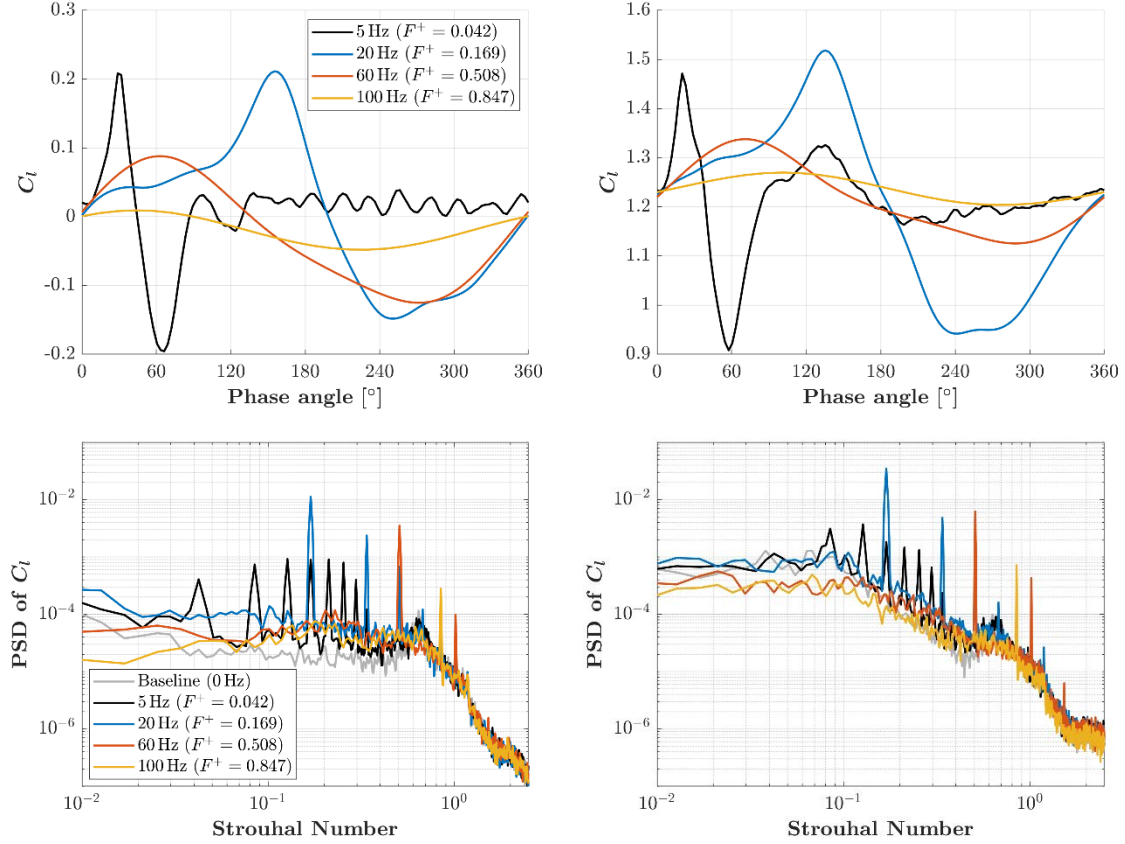


Figure 26: Top: Phase averaged C_l for different forcing frequencies at $\alpha = 0^\circ$ (left) and $\alpha = 16^\circ$ (right). Bottom: Corresponding frequency spectra for the non-phase locked signals.

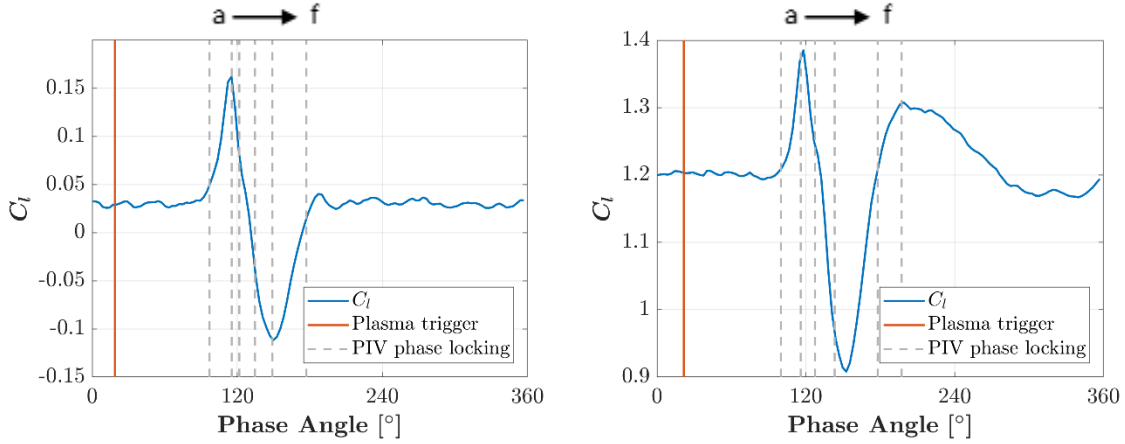


Figure 27: Phase averaged C_l for forcing frequency $F^+ = 0.042$ (5 Hz) at $\alpha = 0^\circ$ (left) and $\alpha = 16^\circ$ (right) indicating locations of PIV and C_p data.

Increasing the target airfoil to $\alpha = 16^\circ$ results in more significant excursions from the mean. In the low frequency case, the C_l rises to nearly 1.5 before falling to 0.9. This is then followed by another more modest increase and decrease in C_l . These latter features are absent from the zero incidence case. The spectrum shows a fundamental frequency and six harmonics. There is also a slight peak near $St = 0.635$ (75 Hz) that is consistent with the baseline case at this angle of attack. This peak is also present in the low frequency spectrum again indicating an isolated encounter. Increasing the VBI frequency to 20 Hz ($F^+ = 0.169$) still results in large excursions, but the signal is becoming more sinusoidal suggesting it is no longer an isolated encounter. The signal is far from sinusoidal as is supported by the spectrum in Figure 27 which now shows 7 harmonics in comparison to the 5 found at zero incidence for this case. Further increases in VBI to $F^+ = 0.508$ (60 Hz) and $F^+ = 0.847$ (100 Hz) show the same trend as in the zero incidence case. $F^+ = 0.508$ (60 Hz) is more sinusoidal having weaker excursions and developing a peak at the fundamental and only one harmonic while $F^+ = 0.847$ (100 Hz) is weaker still having a single peak in the spectrum. In general, the spectra have higher broadband levels for the $\alpha = 16^\circ$ case compared to $\alpha = 0^\circ$ due to the unsteady nature of the flow for this high incidence condition.

It should be noted that the reduced frequency is still rather low at 0.169 (20 Hz). This implies that the horizontal distance between two vortices is roughly six chord lengths. Consequently, an interaction between the individual vortices is not expected to take place. However, the perturbation on the airfoil is not solely limited to the vortex passing over, but also shows some longer-lasting effects. This is in agreement with the convective time of the vortex passing over the target airfoil being about 8 ms (at a convective velocity of $0.9 \cdot U_\infty$), which is equivalent to a phase angle of 14.4° in the $F^+ = 0.042$ (5 Hz) case and 57.6° for $F^+ = 0.169$ (20 Hz).

Until now, the relative location of the wake and target airfoil and more specifically any vortices that create VBI have not been considered. Also, the nature of VBI is not obvious from pressure measurements alone. It is not clear if a viscous response resulting in significant flow separation and vortex shedding occurs. This is now explored using PIV. Given that the response of the flow is most extreme for VBI at $F^+ = 0.042$ (5 Hz), PIV analysis is restricted to this case for now. Figure 28 repeats the low frequency C_l data for both $\alpha = 0^\circ$ and $\alpha = 16^\circ$, but includes dashed vertical lines to indicate the location of presented phase-averaged PIV data for each case.

Phase locking PIV data renders it possible to observe the flow field while displaying synchronized C_p distributions over the airfoil. Figure 28 and Figure 29 show velocity fields on the left-hand side and the pressure coefficient C_p on the right. The plots are for angles of attack of $\alpha = 0^\circ$ and $\alpha = 16^\circ$, respectively. In the C_p plots, the dashed line represents the baseline C_p distribution and serves as a reference. For the PIV

analysis, 250 phase-locked images were recorded and averaged. The background color represents fluctuations (i.e., baseline subtracted) of the transverse velocity component. This highlights the main driver of the C_l perturbation, which is an induced angle of attack due to vortex up- and downwash. The streamlines are drawn on the phase averaged total velocity field.

The influence of induced angle of attack is apparent in the C_l peaks. Figure 28b shows the flow field and surface pressure distribution at C_l maximum for this VBI case. The velocity plot shows a positive transverse velocity fluctuation at the leading edge (induced by vortex upwash) causing an effective positive angle of attack. The streamlines also show the stagnation line of the airfoil moving further down the pressure side. The lift is mainly generated by the first 50% of the airfoil chord.

As the vortex passes over the airfoil, the induced angle of attack decreases due to vortex downwash and the stagnation line moves to the upper surface of the airfoil indicating negative lift. Furthermore, the lines representing the upper and lower surface in the C_p plot flip. A minimum in lift is reached in Figure 28e, where a negative transverse velocity fluctuation is seen at the leading edge. The decrease in C_l mainly originates from the first 50% of the airfoil chord. For the zero incidence case, it can be said that the vortex mainly effects the pressure distribution in the first half of the airfoil chord which is in good agreement with literature (Straus et al. 1990).

The $\alpha = 16^\circ$ case (Figure 29) shows the same general trend as zero incidence case. There is an initial increase in lift that goes along with a positive induced angle of attack, followed by a decrease in lift and a negative induced angle. However, the increase in angle of attack produces separation and shedding of a structure on the suction side, as can be seen in Figure 29b-d. The pressure distribution also shows local regions of zero pressure gradient that move downstream with the separation. The precise mechanism for this has not been examined in detail, but it seems plausible that this is similar to dynamic stall.

Another point distinguishing the $\alpha = 16^\circ$ VBI from the zero incidence case is the aforementioned second (local) lift maximum following the global minimum (see Figure 27). Regarding Figure 29e-f, there again seems to be a positive vertical velocity induced at the leading edge. However, it is significantly lower in amplitude than seen earlier and likely not the main cause for the second peak in C_l . Further examination is required to understand the physics behind this second broader peak. It should be noted that the PIV studies of VBI have been acquired very late and in some cases after the end of the award period. Additional analysis will be provided in an upcoming thesis and AIAA paper.

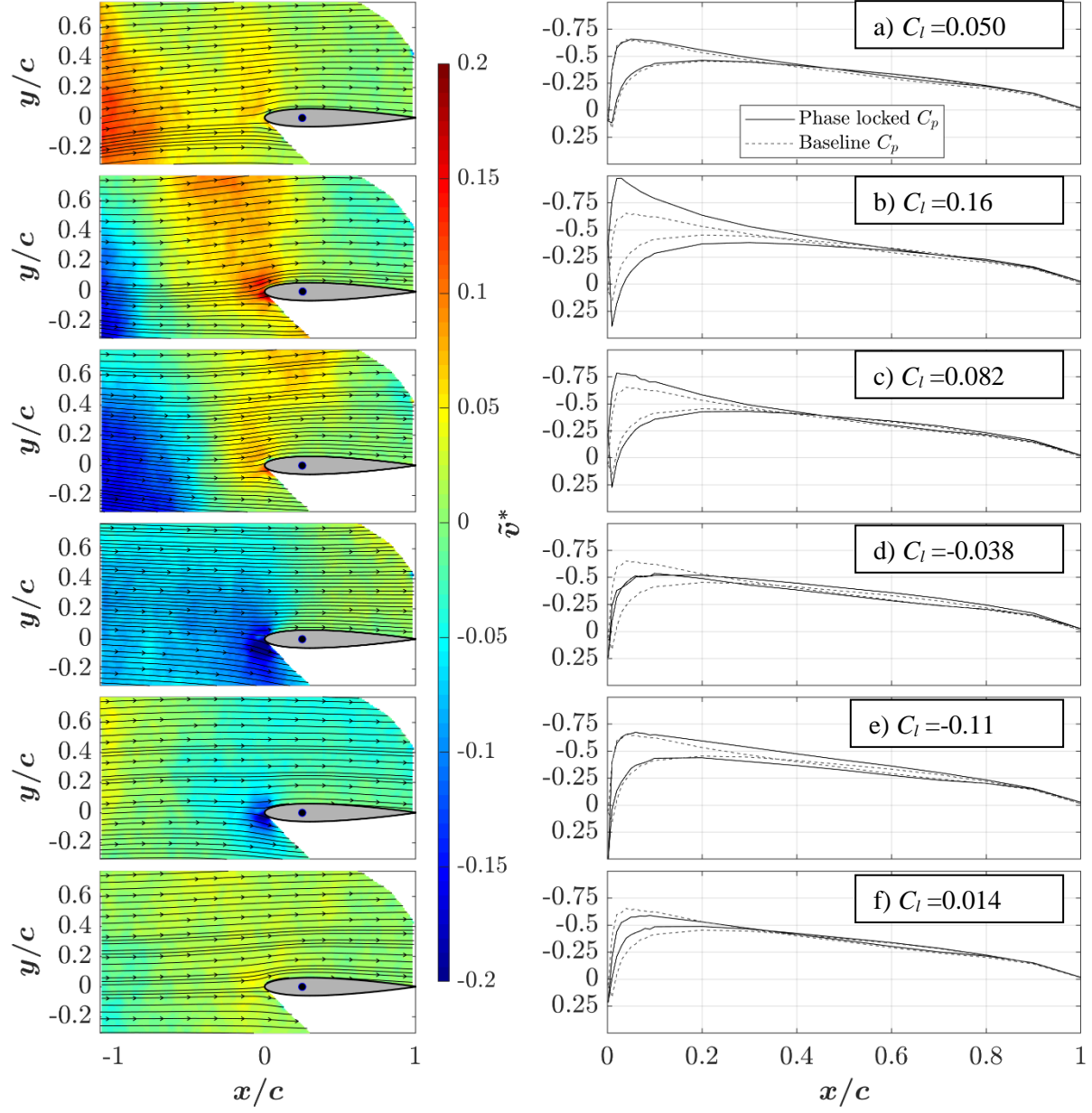


Figure 28: Phase locked PIV images (left) and C_p distributions (right) for $\alpha = 0^\circ$ $F^+ = 0.042$ (5 Hz). Cross reference Figure 27 for a)-f) locations.

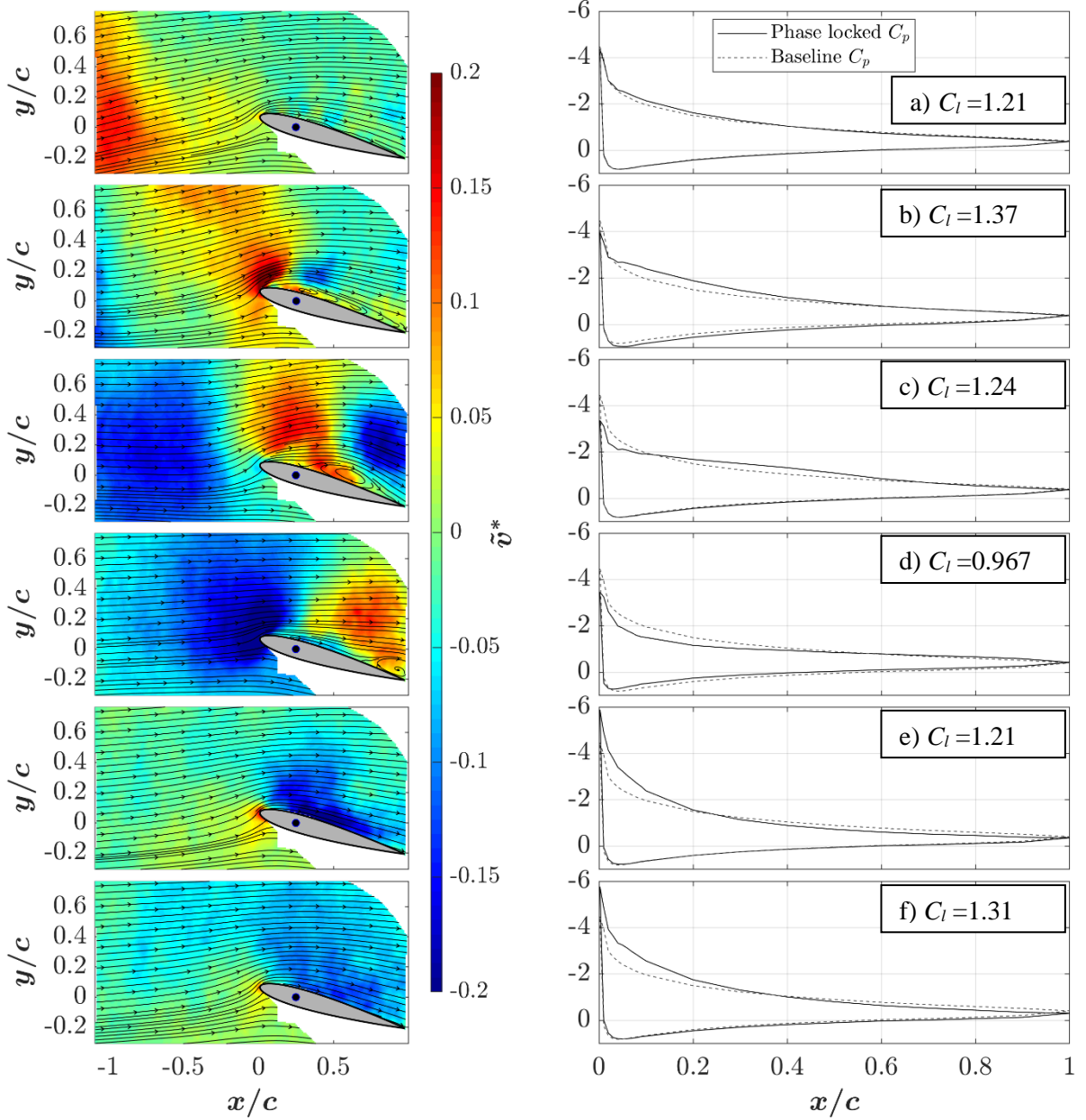


Figure 29: Phase locked PIV images (left) and C_p distributions (right) for $\alpha = 16^\circ$ $F^+ = 0.042$ (5 Hz). Cross reference Figure 27 for a)-f) locations.

VII. Summary and Conclusions

The capability of AFC, specifically ns-DBD plasma actuators, to enable the production of disturbances for studies of VBI has been investigated. Two identical instrumented NACA 0012 airfoils were fabricated to serve as disturbance (upstream) and target (downstream) bodies. The baseline lift coefficient for both airfoils was validated against thin airfoil theory and XFLR5. The disturbance airfoil was positioned at a post-stall angle of 18° . This decision was based on in-house experiments as well as literature suggesting a natural low frequency oscillation can be present in the wake at such conditions (Wu et al. 1998). Ns-DBD plasma actuators were used to excite the separated shear layer over the airfoil as well as the downstream

wake. Low frequency forcing ($F^+ < 0.15$ (20 Hz)) generated a single vortical disturbance after which the flow relaxed back to something resembling the baseline state. The full re-establishment of the baseline separated flow condition was dependent on the frequency of forcing. More specifically, the lowest frequency case (e.g., $F^+ = 0.0375$ (5 Hz)) resembled an impulse response producing multiple higher harmonics in PSD measured at $x/c=6$ from the leading edge of the upstream airfoil. The sign of the vortex in these cases was dominantly positive (counter-clockwise) in the wake indicating it is shed from the pressure surface. Inspection of phase-averaged transverse velocity fluctuations and vorticity from $x/c=0$ to 4.5 showed that a negative region of vorticity (clockwise) is formed by severing the separated shear layer with a single pulse of actuation. However, this structure is weaker and shed into a higher region of the wake such that any VBI is dominated by the interaction of the target airfoil with a single vortex of positive sign (counter-clockwise). The effect of ns-DBD pulse amplitude was explored using single frequency forcing. Results were surprisingly similar to transient separation control studies published using other airfoils, actuators and forcing locations highlighting the robustness of the flow physics (in this case the flow instability) that governs response. A single pulse of actuation severs the separated shear layer resulting in a vortex of negative sign (clockwise) being shed into the wake. The separated flow then gradually re-establishes over approximately 10 convective times in a manner that resembles dynamic stall. Varying the amplitude of forcing by a factor of three did not have an appreciable effect on these observations. This indicates that the effect of frequency and amplitude cannot be decoupled in this particular study of AFC-enhanced VBI. However, this is presumed to be a limitation of the employed power supply rather than some fundamental barrier.

As the ns-DBD forcing frequency is raised ($0.3 < F^+ < 0.92$ ($40 < f < 120$ Hz)), the wake oscillations become sinusoidal. Transverse velocity fluctuations are highly organized into positive and negative patterns associated with a coherent train of vortices. This is also expressed in phase-averaged vorticity where pairs of counter-rotating vortices persist in the wake. PSD at $x/c=6$ show a single dominant peak consistent with this signal. A further increase in forcing frequency results in separation control over the disturbance airfoil with no clear structure in the wake. This is expected for a forcing frequency near $F^+ \approx 1$ based on knowledge of boundary layer separation control (Greenblatt and Wygnanski 2000) and the fact that the wake is not clearly excited is not surprising. All forcing frequencies have an influence on the time-average velocity and surface pressure, but it is clear throughout the data that $F^+ \approx 1.14$ (120 Hz) is optimal for separation control in these conditions. The time-average flow over the disturbance airfoil under the influence of AFC is reasonably two-dimensional over the central half-span based on surface pressure measurements. The coherence of AFC generated disturbances is found to reach levels well-above 0.5 at $x/c=6$ across the central half of the wake suggesting some level of 2D behavior. In general, the wake can be excited at any frequency (at least downstream to $x/c=6$) provided it is near or below the onset of the inertial subrange. More specifically, forcing below $F^+ < 0.15$ (20 Hz) produces a single disturbance that is dominated by positive vorticity and appears at the fundamental frequency and multiple harmonics in the PSD. The wake can be locked to a single frequency in the range ($0.3 < F^+ < 0.92$ ($40 < f < 120$ Hz)) characterized by sinusoidal behavior and a single peak in the PSD. At higher frequencies, the disturbance airfoil experiences boundary layer separation control and forcing is not relevant for AFC-enabled VBI studies.

VBI is explored for each of the previously mentioned forcing regimes. The effect of the baseline wake from the disturbance airfoil on the lift coefficient of the target airfoil is to eliminate the onset of hard stall presumably due to accelerated laminar-to-turbulent transition. A natural unsteadiness in C_l is found for this case near $St=0.635$ (75 Hz). Note that expressions of F^+ and St employ the characteristic velocity of the wake in reference to VBI studies here. Thus, the dimensionless frequencies are increased by 10% compared the case with a disturbance airfoil alone. The most compelling force and momentum fluctuations due to VBI on the target airfoil are found for isolated encounters ($F^+ \leq 0.169$ (20 Hz)) at high incidence (e.g., 16°). In this case, a clear viscous response is observed on the target airfoil that results in formation and shedding of a separation bubble. This produces an abrupt increase and subsequent decrease in lift coefficient followed by another broader increase during the lift recovery. The cause of the latter is still under investigation. PSD of C_l show a peak at the fundamental frequency along with multiple higher harmonics. Increasing the frequency (non-isolated encounter) or decreasing the loading (lower AoA) eliminates this

effect and generates nearly sinusoidal behavior of the target airfoil lift coefficient that could likely be modeled with potential flow. The upwash and downwash produced by the various vortices is quite clear from phase-averaged PIV and explains the variations in C_l in most cases.

VIII. Future Work

The utility of AFC for enhancing studies of VBI has been demonstrated, but full development of this capability requires further investigation. The following topics are suggested.

- The strength of the AFC-generated vortex should be quantified using a vortex Reynolds number or some other accepted definition. This should be coupled with frequency and trajectory to fully characterize the disturbance.
- The location of the target airfoil relative to the disturbance airfoil should be varied in both the streamwise and transverse directions to evaluate different vortex trajectories and their effect on VBI.
- VBI at higher Mach and Reynolds number should be investigated. This specific work employed ns-DBD plasma actuators for disturbance generation, but other flow control devices may serve the same purpose provided control authority can be achieved. It is well-known that AFC amplitude requirements for zero net mass flux (ZNMF) momentum-based flow control actuators (e.g., ac-DBD plasma, synthetic jets) scale with freestream velocity or dynamic pressure (Seifert and Tilmann 2009). Thus, their utility for high-speed flow control is sometimes questionable. The full capability of ns-DBD plasma actuators for enhancing VBI research lies in studies of higher speed (likely compressible subsonic) flow conditions where ZNMF fluidic actuators are less likely to influence the flow.
- The effect of ns-DBD pulse amplitude is minimal in the range surveyed, but recent literature suggests it will have an influence provided a more capable power supply is employed (Komuro et al. 2018). This may allow one to de-couple the AFC-generated VBI amplitude from frequency.
- The disturbances should be tuned to a specific application by using different disturbance models (e.g., airfoils and or other cross sections of varying size and shape).
- 3D VBI studies should be considered by varying the forcing strategy, disturbance body or disturbance/target orientation.
- AFC of VBI should be examined and prospects for new or optimized control strategies should be investigated.

IX. Publications and Students

To date, the research project produced 1 conference abstract, 2 conference papers and 2 MS theses. One conference paper, one MS thesis and one journal article are in preparation. A list of the publications is provided below.

Conference Abstracts

1. C. Durasiewicz, J. Maldonado and J. Little, "Active Control of Airfoil Boundary Layer Separation and Wake using Ns-DBD Plasma Actuators," 69th American Physical Society, Division of Fluid Dynamics Meeting, Portland, OR, November 21, 2016; Bulletin of the American Physical Society, Vol. 61, No. 20.

Conference Papers

1. T. Ashcraft, K. Decker and J. Little. "Control of Boundary Layer Separation and the Wake of an Airfoil using ns-DBD Plasma Actuators", 54th AIAA Aerospace Sciences Meeting, AIAA SciTech Forum, (AIAA 2016-0839).
2. C. Durasiewicz, A. Singh and J. Little. "A Comparative Flow Physics Study of Ns-DBD vs Ac-DBD Plasma Actuators for Transient Separation Control on a NACA 0012 Airfoil", 2018 AIAA Aerospace Sciences Meeting, AIAA SciTech Forum, (AIAA 2018-1061)
3. A. Weingaertner, P. Tewes and J. Little. "Parallel Vortex Body Interaction Enabled by Active Flow Control", submitted to the 2018 AIAA Aviation Meeting.

Journal Articles

1. T. Ashcraft, C. Durasiewicz, A. Singh, K. Decker and J. Little, “Airfoil Post-Stall Flow Control using ns-DBD Plasma Actuation (*tentative*)” in preparation for submission to Experiments in Fluids, 2018.

MS Theses

1. T. Ashcraft, “Control of Boundary Layer Separation and the Wake of an Airfoil using Ns-DBD Plasma Actuators,” MS Thesis, Aerospace and Mechanical Engineering, University of Arizona, 2016.
2. C. Durasiewicz, “Comparison of Transitory Separation Control over an Airfoil using Ac-DBD and Ns-DBD Plasma Actuators,” MS Thesis, TU Berlin, 2017.
3. A. Weingaertner, “Parallel Vortex Body Interaction Enabled by Active Flow Control,” MS Thesis, TU Berlin, expected 2018.

Students Supported

- T. Ashcraft, MS 2016 (external support)
C. Durasiewicz, MS 2017
A. Singh, PhD expected 2019 (partial support)
A. Weingaertner, MS expected 2018

X. Acknowledgements

This work has been supported by the U.S. Army Research Office Young Investigator Program (W911NF-14-1-0662 monitored by Dr. Matthew Munson), U.S. Army Research Office High School Apprenticeship Program/University Research Apprenticeship Program, Arizona-NASA Space Grant Consortium, Department of Aerospace and Mechanical Engineering and the College of Engineering at the University of Arizona. Timothy Ashcraft was supported by the Army Advanced Civil Schooling Program and the Civil and Mechanical Engineering Department at the United States Military Academy. Fabrication of one NACA 0012 model was made possible by a University of Arizona Faculty Seed Grant and carried out as part of an Aerospace Engineering Undergraduate Senior Design Project by Cesar Barroso, David Dones, Lee Ficke, George Gudgeon, Andrew McGuckin and Nathan Turner. The initial foundation of the research effort was carried out by Marcel Dengler during his Bachelors thesis as a visiting student from TU Berlin. The authors also wish to thank Jorge Maldonado, Zack Wellington, Sebastian Endrikat, Philipp Tewes, Dale Drew and Lane Hammond for their assistance.

XI. References

- Akins D, Singh A, Little J (2015) Effects of Pulse Energy on Shear Layer Control using Surface Plasma Discharges. AIAA Paper 2015-3344
- Albrecht T, Weier T, Gerbeth G, Monnier B, Williams D (2015) Separated Flow Response to Single Pulse Actuation. AIAA Journal 53[1]:190-199
- Amitay M, Glezer A (2002) Controlled transients of flow reattachment over stalled airfoils. International Journal of Heat and Fluid Flow 23[5]:690-699
- Amitay M, Glezer A (2006) Flow Transients induced on a 2D Airfoil by Pulse-modulated Actuation. Experiments in Fluids 40:329-331
- Bergh H, Tijdeman H (1965) Theoretical and experimental results for the dynamic response of pressure measuring systems, Amsterdam: Nationaal Lucht-En Ruimtevaartlaboratorium (National Aero- and Astronautical Research Institute)
- Booth E (1990) Experimental observations of two-dimensional blade-vortex interaction. AIAA Journal 28[8]:1353-1359

- Booth ER, Yu JC (1986) Two-dimensional blade-vortex flow visualization investigation. *AIAA Journal* 24[9]:1468-1473 DOI 10.2514/3.9467
- Brzozowski DP, K. Woo GT, Culp JR, Glezer A (2010) Transient Separation Control Using Pulse-Combustion Actuation. *AIAA Journal* 48[11]:2482-2490 DOI 10.2514/1.45904
- Darabi A, Wygnanski I (2004a) Active management of naturally separated flow over a solid surface. Part 2. The separation process. *Journal of Fluid Mechanics* 510:131-144
- Darabi A, Wygnanski I (2004b) Active Management of Naturally Separated Flow over a Solid Surface. Part 1. The Forced Reattachment Process. *Journal of Fluid Mechanics* 510:105-129
- Dawson R, Little J (2013) Characterization of nanosecond pulse driven dielectric barrier discharge plasma actuators for aerodynamic flow control. *Journal of Applied Physics* 113[10]:103302-103310
- Doligalski TL, Walker JDA (1984) The boundary layer induced by a convected two-dimensional vortex. *Journal of Fluid Mechanics* 139:1-28 DOI doi:10.1017/S0022112084000240
- Durasiewicz C, Singh A, Little JC (2018) A Comparative Flow Physics Study of Ns-DBD vs Ac-DBD Plasma Actuators for Transient Separation Control on a NACA 0012 Airfoil. In: 2018 AIAA Aerospace Sciences Meeting: American Institute of Aeronautics and Astronautics
- Enloe C, McLaughlin T, VanDyken R, Kachner K, Jumper E, Corke T, Post M, Haddad O (2004) Mechanisms and Responses of a Single Dielectric Barrier Plasma Actuator: Geometric Effects. *AIAA Journal* 42[3]:595-604
- Favier D, Castex A, Maresca C (1985) Unsteady characteristics of an airfoil interacting with a vortical wake. *AIAA Paper* 1985-1707
- Greenblatt D, Wygnanski I (2000) The Control of Flow Separation by Periodic Excitation. *Progress in Aerospace Sciences* 36:487-545
- Gursul I, Rockwell D (1990) Vortex street impinging upon an elliptical leading edge. *Journal of Fluid Mechanics* 211:211-242 DOI doi:10.1017/S0022112090001550
- Hardin J, Lamkin S (1987a) An Euler code calculation of blade-vortex interaction noise. *Journal of Vibration, Acoustics, Stress and Reliability in Design* 109:29-36
- Hardin JC, Lamkin SL (1987b) Concepts for reduction of blade/vortex interaction noise. *Journal of Aircraft* 24[2]:120-125 DOI 10.2514/3.45428
- Horner MB, Galbraith RAM, Coton FN, Stewart JN, Grant I (1996) Examination of vortex deformation during blade-vortex interaction. *AIAA Journal* 34[6]:1188-1194 DOI 10.2514/3.13211
- Howe M (1995) On the force and moment on a body in an incompressible fluid, with application to rigid bodies and bubbles at high and low Reynolds numbers. *The Quarterly Journal of Mechanics and Applied Mathematics* 48[3]:401-426 DOI 10.1093/qjmam/48.3.401
- Jukes T, Choi K, Johnson G, Scott S (2006) Characterization of Surface Plasma-Induced Wall Flows Through Velocity and Temperature Measurements. *AIAA Journal* 44[4]:764-771
- Komuro A, Takashima K, Suzuki K, Kanno S, Bhandari S, Nonomura T, Kaneko T, Ando A, Asai K (2018) Evaluation of discharge energy and lift recovery of NACA0015 airfoil controlled by nanosecond-pulse-driven plasma actuator. In: 2018 AIAA Aerospace Sciences Meeting: American Institute of Aeronautics and Astronautics
- Lee DJ, Smith CA (1991) Effect of vortex core distortion on blade-vortex interaction. *AIAA Journal* 29[9]:1355-1362 DOI 10.2514/3.10746
- Lee S, Bershader D (1994) Head-on parallel blade-vortex interaction. *AIAA Journal* 32[1]:16-22
- Lee T (2011) Flow past two in-tandem airfoils undergoing sinusoidal oscillations. *Experimental Fluids* 51:1605-1621
- Leishmann JG (2000) *Principles of Helicopter Aerodynamics* Cambridge, UK: Cambridge University Press
- Little J (2018) Localized Thermal Perturbations for Control of Turbulent Shear Flows. *AIAA Journal* invited submission to the Special Issue on Flow Control
- Little J, Takashima K, Nishihara M, Adamovich I, Samimy M (2012) Separation Control with Nanosecond-Pulse-Driven Dielectric Barrier Discharge Plasma Actuators. *AIAA Journal* 50[2]:350-365
- Maresca C, Favier D (1984) Experimental study and modeling of the influence of a periodic wake on a lifting surface. *AIAA Paper* 1984-1660

- Mathis R, Collin E, Delville J, Bonnet JP (2007) Analysis of a plane turbulent mixing layer manipulated by a localized forced separation. *Journal of Turbulence* 8[56]:1-14
- Mathis R, Lebedev A, Collin E, Delville J, Bonnet J (2009) Experimental Study of Transient Forced Turbulent Separation and Reattachment on a Bevelled Trailing Edge. *Experiments in Fluids* 46:131-146
- Meier G, Timm R (Year) Unsteady vortex airfoil interaction. In: *Unsteady Aerodynamics - Fundamentals and Applications to Aircraft Dynamics*
- Merrill BE, Peet YT (2017) Effect of Impinging Wake Turbulence on the Dynamic Stall of a Pitching Airfoil. *AIAA Journal* 55[12]:4094-4112 DOI 10.2514/1.J055405
- Panaras A (1987) Numerical modeling of the vortex/airfoil interaction. *AIAA Journal* 25[1]:5-11
- Poling DR, Dadone LEO, Telionis DP (1989) Blade-vortex interaction. *AIAA Journal* 27[6]:694-699 DOI 10.2514/3.10167
- Rethmel C, Little J, Takashima K, Sinha A, Adamovich I, Samimy M (2011) Flow Separation Control using Nanosecond Pulse Driven DBD Plasma Actuators. *International Journal of Flow Control* 3[4]:213-232
- Rival D, Manejev R, Tropea C (2010) Measurement of parallel blade-vortex interaction at low Reynolds numbers. *Experiments in Fluids* 49:89-99
- Rockwell D (1998) Vortex-Body Interactions. *Annual Review of Fluid Mechanics* 30:199-229
- Roupasov D, Nikipelov A, Nudnova M, Starikovskii A (2009) Flow Separation Control by Plasma Actuator with Nanosecond Pulsed-Periodic Discharge. *AIAA Journal* 47[1]:168-185
- Seath D, Kim J-M, Wilson DR (1989) Investigation of the parallel blade-vortex interaction at low speed. *Journal of Aircraft* 26[4]:328-333 DOI 10.2514/3.45764
- Seifert A, Tilmann C (2009) Fixed Wing Airfoil Applications. In: *Fundamentals and Applications of Modern Flow Control*. eds Joslin, R and Miller, D). Vol. 231, pp. 231-257, Reston, VA: AIAA
- Straus J, Renzoni P, Mayle R (1990) Airfoil pressure measurements during a blade vortex interaction and a comparison with theory. *AIAA Journal* 28[2]:222-228
- Sung Y, Kim W, Mungal M, Cappelli M (2006) Aerodynamic Modification of Flow over Bluff Objects by Plasma Actuation. *Experiments in Fluids* Vol. 41:479-486
- Swirydczuk J, Wilder M, Telionis D (1993) The interaction of coherent vortices with thin flat plates. *Journal of Fluids Engineering* 115:590-596
- Takashima K, Zuzek Y, Lempert W, Adamovich I (2011) Characterization of a Surface Dielectric Barrier Discharge Plasma Sustained by Repetitive Nanosecond Pulses. *Plasma Sources Science and Technology* 20[055009]
- Tucker B, Conlisk A (1992) Massive vortex motion in the presence of solid boundaries. *Physics of Fluids A* 4:290-305
- Wilder M, Telionis D (1998) Parallel Blade-Vortex Interaction. *Journal of Fluids and Structures* 12:801-838
- Williams DR, Tadmor G, Colonius T, Kerstens W, Quach V, Buntain S (2009) Lift Response of a Stalled Wing to Pulsatile Disturbances. *AIAA Journal* 47[12]:3031-3037 DOI 10.2514/1.45407
- Williamson C (1996) Vortex dynamics in the cylinder wake. *Annual Review Fluid Mechanics* 28:477-539
- Wu J, Lu X, Denny A, Fan M, Wu J (1998) Post-stall Flow Control on an Airfoil by Local Unsteady Forcing. *Journal of Fluid Mechanics* 371:21-58
- Yao Z, Liu D (1998) Vortex dynamics of blade-blade interaction. *AIAA Journal* 36[4]:497-504